Article

Not peer-reviewed version

# Computational Fluid Dynamics Modeling of Pack-Level Battery Thermal Management Systems in Electric Vehicles

Yifan Chen and Zhong Hu *

Posted Date: 13 January 2025

doi: 10.20944/preprints202501.0859.v1

Keywords: Electric vehicle; Battery thermal management system; Air and liquid cooling; Computational fluid dynamics; Battery pack

Preprints.org (www.preprints.org) | NOT PEER-REVIEWED | Posted: 13 January 2025 doi:10.20944/preprints202501.0859.v1

*Article*

# Computational Fluid Dynamics Modeling of Pack-Level Battery Thermal Management Systems in Electric Vehicles

**Yifan Chen and Zhong Hu ***

Department of Mechanical Engineering, J.J. Lohr College of Engineering/Brookings, South Dakota State University, Brookings, SD57007, USA

* Correspondence: author, email: Zhong.hu@sdstate.edu and Phone: +1-605-688-4817 (O)

**Abstract:** Electric vehicles (EVs) are considered as a primary choice for environmentally friendly transportation. Among the current available battery types, lithium-ion (Li-ion) batteries are the most favored by car companies. Li-ion batteries are rechargeable with high energy storage density and tend to generate excess heat during operation. In EVs, the batteries are arranged in the battery pack (BP), which has a small layout space and difficulty in dissipating heat. Therefore, in EVs, the battery thermal management systems (BTMSs) are critical to manage heat to ensure safety and performance, particularly under higher operating temperatures and longer discharge conditions. To solve this problem, in this article, the thermal analysis models of a 3-battery-cell BP were created, including natural air cooling without a BTMS, natural air cooling with water cooling hybrid BTMS, and forced air cooling plus water cooling composite BTMS. The thermal performances of the pack-level BPs were simulated and analyzed based on computational fluid dynamics (CFD). A variety of boundary conditions and working parameters, such as ambient temperature, inlet coolant flowrate and initial temperature, discharge rate, air flowrate and initial temperature, were considered. The results show that without a BTMS, the temperature in the BP rises rapidly and continuously to above the recommended operating temperature range (ROTR) under the discharge rate of 2C or above. With a hybrid BTMS, the temperature in BP is slightly above the ROTR. While with a composite BTMS, the temperature is within the ROTR. In addition, lowering the initial coolant temperature or air temperature can effectively decrease the temperatures in BP. Finally, the thermal performances of the different battery cells in the BP with different cooling systems and at the different positions of the BP were compared and analyzed. The present work may contribute to the design of BTMSs in the EV industry.

**Keywords:** electric vehicle; battery thermal management system; air and liquid cooling; computational fluid dynamics; Battery pack

## 1. Introduction

Global fossil $CO_2$ emissions are expected to further increase in 2023 by 1.1% relative to 2022, reaching 36.8 Gt $CO_2$ $yr^{-1}$[1]. In this regard, it is worth noticing that the automobile industry is one of the key contributors since the number of automobiles, particularly motor vehicles, is estimated to reach 1.47 billion by 2023 at the latest [2]. Therefore, there is increasing concern about the causes and effects of global warming and climate change. There are growing calls to reduce carbon emissions. Electric vehicles (EVs) cannot emit greenhouse gases during operation, and it has the potential benefit of reducing daily tailpipe emissions compared to the conventional carbon-based fuel vehicles. Thus, the EV market is seeing exponential growth [3]. The projected EV demands in major automotive markets will have a profound impact on the current environment policy on energy markets and climate goals. Under the International Energy Agency's Stated Policies Scenario (STEPS), the predicted global share of EV sales has risen from less than 25% in previous forecasts to 35% by 2023, based on the existing policies and company targets. China remains the largest market for EVs in the forecast, accounting for 40% of total sales by 2030. Thanks to recent policy moves, the US market share will double to 20% by the end of the decade, while Europe's market share will maintain at 25% [3].

EVs are divided into two categories: pure EVs and hybrid EVs. The former only uses electrical energy as a power source, while the latter uses a conventional gasoline engine running in parallel with a power battery. Pure EVs are more environmentally friendly than hybrid EVs, but usually have shorter battery life. Currently, the mileage of EVs is difficult to reach the level of carbon-based fuel vehicles at the same price. Therefore, the type of battery for EVs becomes a critical issue.

At present, the main requirements for EVs are long battery life and extended battery cycles. These two aspects require the EVs' batteries to have high energy density, prolonged cycle periods, and high discharge rates. The most common choice in the current EV market is lithium-ion (Li-ion) batteries. Compared with other rechargeable batteries, the Li-ion batteries show superior advantages, including low mass density, low self-discharge rate, high energy density, and great working performance. Li-ion batteries are a balanced choice [4]. However, in low-temperature conditions, the loss of energy in batteries primarily arises from the precipitation of Li-ions within Li-ion batteries, forming Li-dendrites. These Li-dendrites may penetrate the battery's membrane, leading to short internal circuits and resulting in energy loss [5]. Studies have shown that excessive environmental temperatures can induce irreversible thermal runaway in batteries. This leads to the oxidation of the electrolyte (chemical reactions, resulting in electrolyte decomposition) and the release of large amounts of gas, causing rapid expansion of the batteries, intensifying internal side reactions, generating significant heat, and thereby triggering safety incidents such as self-ignition and explosions [6,7]. Furthermore, temperature variations directly impact the discharge performance and capacity of Li-ion batteries. Both elevated temperatures (≥50°C) and low temperatures (≤20°C) can cause varying degrees of capacity reduction in Li-ion batteries [8]. Research indicates that after 500 discharge cycles at 55°C, the capacity of Li-ion batteries drops by nearly 70% [9]. Considering the EV target market and seasonal ambient temperatures, it was determined that the operating temperature of the battery pack (BP) should be between -30°C and +50°C. The battery cells within a BP often exhibits uneven temperatures. Poor temperature uniformity can lead to partial state of charge (SOC), which reduces the cycle life of the batteries [10,11]. Therefore, the recommended operation temperature range (ROTR) of a BP should be maintained between +20°C to +35°C [12].

Research and applications clearly show that temperature is a key factor affecting the performance of Li-ion batteries, limiting the application of Li-ion batteries [13]. Furthermore, the battery capacity degradation (leading to battery failure) is affected by several factors including temperature, current and voltage during charging and discharging operations, and the level at which the battery is charged and discharged.

In EVs, the batteries are arranged in the BP, which has a small layout space and difficulty in dissipating heat. Therefore, in EVs, the battery thermal management systems (BTMSs) have a significant impact on their performance [14]. Thus, accurate prediction of temperature inside Li-ion batteries and effectively design and optimize the BTMS are crucial. In this study, three-dimensional models of three-battery-cell pack-level BP, including a BP model without a BTMS (with surface natural air convection cooling only), or a BP model with a hybrid BTMS (surface natural air cooling plus liquid (water) cooling), and a BP model with a composite BTMS (with forced air cooling plus a liquid (water) cooling), were generated. The commercial software ANSYS® Fluent was used to perform numerical simulations on the thermal performance of the pack-level BP models based on computational fluid dynamics (CFD). The effects of parameters, including ambient temperature, inlet coolant flowrate and initial temperature, discharge rate, air flow rate and initial temperature, on the thermal behaviors of the BPs were analyzed. Finally, the thermal performances of the single battery cells in BP with different cooling systems and at the different positions in the BP were compared and analyzed.

## 2. Battery Thermal Management Systems (BTMSs)

In extreme temperature operating environments, problems such as electrolyte performance degradation and thermal runaway can occur in Li-ion batteries [15]. Therefore, it is necessary to integrate the BTMS into the BP so that to be able to keep the BP' operating temperature within a safe range [16], i.e., to effectively control the heat generation, heat dissipation, and temperature distribution of the BPs during battery charge-discharge operation cycles. Thus, the BTMSs serve as an important means and can effectively extend the lifespan of the Li-ion batteries, improve the performance, cost per power output, safety of the batteries by adjusting the temperature levels and the distribution of the batter layout and the BTMS design in the EVs [16–19].

In order to keep the BP in the EVs within the optimal operating temperature range, i.e., ROTR, the BTMS needs to perform several functions: dissipating the generating heat during battery charging and discharging operation, preventing sudden changes in temperature by system thermal insulation, and ventilating to remove potentially harmful gases from the operation. The BTMSs with evolution of EV battery technology, such as increased in power capacity, voltage, and current in proportion to increased range requirements, become a critical system. The requirements of the BTMS also include small overall system weight, minimal space occupancy within the vehicle, simple structure, and avoidance of multi-step or complex production processes [20,21]. Based on the cooling methods employed, BTMSs can be categorized into three primary types, i.e., active cooling, passive cooling, and hybrid cooling. Figure 1 shows the detailed categorization of the commonly adopted BTMSs [22–24].

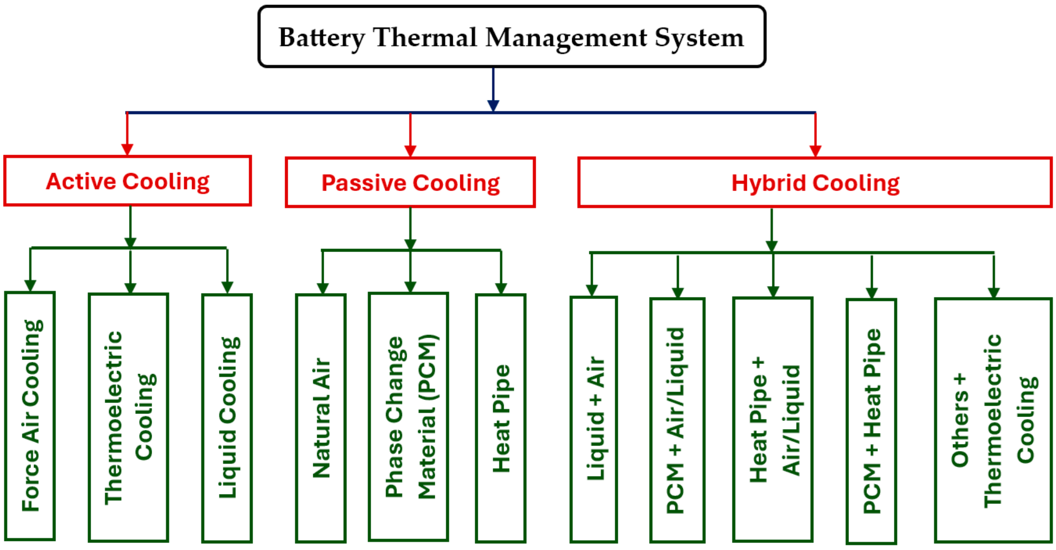

**Figure 1.** Schematic diagram of BTMS classifications.

In the class of active cooling BTMSs, forced air cooling, fluid cooling, and thermoelectric cooling are included. For forced air cooling, the batteries are placed in a housing, and air is forced to pass through the BP and cools the batteries. The method can use filtered and cooled waste cabin air. Thus, the heat convection between the batteries and air can be controlled by the fan speed. So, the impact on the power consumption and cruising range of the entire auxiliary system is significantly smaller. For fluid cooling, it needs to move a liquid (such as a coolant) with heat transfer ability over the batteries to dissipate the heat from the batteries. The heat dissipation ability of a coolant depends on the characteristics of the coolant itself and the working conditions, such as viscosity (flow ability), density (specific heat), thermal conductivity (heat conduction ability), fluid temperature and flowrate (working conditions), etc. The coolant is usually a variant of ethylene glycol. Forced air convection is also possible between air and liquid cooling through a heat exchanger. Thermoelectric cooling is based on the Peltier effect, has moving parts and no vibration, and is small in size. The cooling effect can be adjusted through controlling the current.

In the passive cooling BTMS category, it includes natural air cooling, phase change material cooling, and heat pipe cooling. For the natural air cooling (convection), the air moves through the BP due to changes in air density. No power consumption is needed as there is no pump, fan, or compressor needed in the system. Therefore, it is the simplest cooling form, but it is not very efficient as it only works under certain conditions and it greatly depends on the outside air temperature, and it works better as if the air flowrate is controlled by a fan. For phase change material (PCM) cooling, a solid/liquid phase interchange material is encapsulated next to the battery cells. The temperature enabling the material phase changing is usually between 50 and 70°C so that it can absorb heat from the overheated batteries. While the heat pipe cooling system has two ends, one end absorbs heat by the liquid medium by the liquid wick and turns into vapor. The other end gives off heat and turns back vapor into liquid medium through condensation. Therefore, the liquid medium moves from the condensation end to the evaporation end, while the vapor moves in the opposite way.

In the class of hybrid cooling BTMSs, they are just combinations of the above active and passive cooling systems. It has shown that hybrid BTMSs will be one of the promising technologies soon [25–27]. At present, the existing BTMSs have their own advantages and disadvantages. Researchers have begun to develop new BTMSs by using new coolants, changing the system structure, and other novel design methods [28–35].

## 3. Method and Model Used for Evaluating BTMSs

It is crucial to effectively evaluate the performance and thermal behavior of Li-ion batteries during operation. Various factors and operational parameters, such as electrochemistry, operation time, ambient temperature, discharge rate, and charging status, type of coolant, coolant temperature and flow rate, influence battery performance, heat generation, and heat dissipation. These factors pose challenges for researchers in accurately determining current density within the battery and the non-uniformity of battery surface temperature during instantaneous transient conditions. For example, in a free convection airflow setup, the maximum temperature difference for a single cell exceeded 2°C, while in a forced convection airflow configuration, it exceeded 3°C, even though the average temperature is lower [36]. Studies have found that the conductivity of the solid phase and liquid phase will affect the current density, thereby affecting the electrochemistry of the batteries, and the uniformity of the current density distribution is related to the utilization of active materials in the electrode [37].

### *3.1. Experimental and Computational Methods for Evaluating BTMSs*

In order to evaluate the BP's performance in an EV, several experimental methods, especially non-destructive techniques, can be adopted, such as (1) Electromechanical impedance spectroscopy (EIS) measures battery impedance as a function of the input frequencies. Since impedance is a measure of a battery's resistance to the flow of current. EIS can be used to evaluate a few batteries' performance related to SOC to gain insight into the properties of the BP system; (2) Infrared Thermography (IRT) can be used for quality control and process monitoring. An IRT is equipped with an infrared camera enabling temperature measurement by capturing the infrared spectrum emitted by the measuring surfaces; (3) X-ray computer tomography (XCT) examines internal structures and gain insight into the mechanical and structural stability and damage of the BP system. This technique is widely used in medical imaging for diagnosing diseases and injuries, and in the materials science and engineering to examine the internal structure and damage of objects without causing damage; (4) Ultrasonic testing (UT) used in Li-ion battery evaluation mainly focuses on detecting defects and monitoring the battery's SOC and health status in real time. It emits the ultrasonic waves to propagate in the battery material receives the waves reflecting from the interface between components such as electrodes and electrolytes [38]; (5) Of course, the simplest thermocouples can be installed on the battery surface to monitor changes in battery surface temperature during battery operation; (6) Isothermal battery calorimeters and acceleration calorimeters can be used to measure heating rates. Isothermal battery calorimeters are ideal for assessing continuous heating, but face challenges in capturing transient temperature in batteries. This method only works if the battery surface temperature is consistently uniform. On the other hand, acceleration calorimeters are more commonly used to monitor battery temperatures during thermal runaway experiments because they can effectively measure battery discharge temperature [39,40].

The BTMSs in EVs are expected to perform a variety of functions, such as measuring basic system operation conditions such as voltage, temperature, and current of the BP system. However, to accurately determine the availability of energy in order to reliably calculate the range, complex algorithms are needed. Although, each battery in a parallel BP can maintain the same voltage, the batteries in series during operation can have different voltages even if they are identical. Since batteries at different locations within BP are subject to different environmental conditions and also small differences in the manufacturing process accumulate over time. These factors may result in the capacity decay of the series batteries. This shows that the BTMS is an important component to the energy storage system, and effective and accurate evaluation and analysis of the BTMS is a prerequisite for the overall optimal design of the BTMS [41].

From previous experimental studies, there is a lack of quantitative evaluation and comprehensive understanding of the effects of various working conditions/parameters and their interaction in BTMS on BP performance. Traditional trial-and-error based experimental methods are costly, time-consuming, and sometimes even impossible. Computer simulations can evaluate the thermal performance of the designed BTMS, including the thermal performance of the batteries during charging and discharging, and the size of the passive and active cooling elements. Depending on the problem interest and the simulation capability, various approaches for evaluation and optimal design of the performance of the BTMS based on computer modeling are evolving, ranging from subatomic scales (such as quantum mechanics), atomic scales (such as molecular dynamics), to micro and macro scales (such as continuum mechanics based finite element analysis (FEA) and computational fluid dynamics (CFD)) [41]. In general, by establishing mathematical and physical models and equations for multi-field coupling analysis of battery systems and selecting appropriate meshes, CFD simulation method can be used for extensive preliminary experiments, thus offering optimized solutions for various aspects of battery performance. The commercial software ANSYS®, a versatile software, within the CFD software ANSYS Fluent, includes a Li-ion battery module which can be used to simulate the performance of the BTMSs.

The battery thermal model is one of the models used to evaluate the thermal performance of the BTMS, taking into account the factors such as the battery's heat generation characteristics, surface thermal uniformity, and the battery's maximum, minimum, and average temperatures.

### *3.2. Fundamentals of CFD and Thermal Models of BTMS in This Study*

In this work, the 3-battery cell pack-level thermal BP models, including a surface natural air (passive) cooling without a BTMS, a surface natural air cooling with a fluid (water) cooling hybrid BTMS, and a surface forced air cooling plus a fluid (water) cooling composite BTMS, relative simpler battery cooling systems by which the cooling performance can be manipulated or optimized, were created and studied based on ANSYS® Fluent CFD simulations. These BP models consist of four thermally conductive silicon plates (each one placed above, below, and between the batteries), two liquid cooling aluminum plates (have squared cooling cannels above and below the thermally conductive silicon plates which are above and below the batteries), and two aluminum shells on both sides of the batteries. The entire system adopts an incomplete encapsulation structure for air passing through and coolant circulation. The BP shell is constructed from aluminum plates, a good conductive material. Figure 2 illustrates the designed geometric model having surface air or forced air and fluid cooling BTMS.

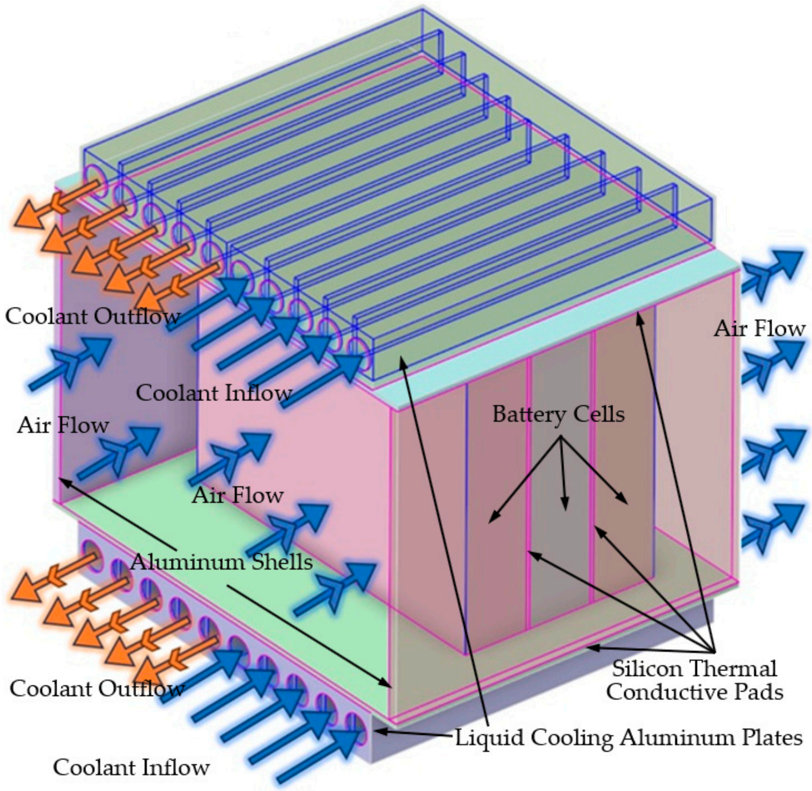

**Figure 2.** Perspective view of the BP structure with the designed BTMS.

Since the coolant flow in this designed model is turbulent, the commonly used turbulent model in CFD is the standard k-ε model. This method is based on the concept of eddy viscosity. In this type of turbulence model, two transport equations, i.e., the turbulent kinetic energy k and the turbulent eddy dissipation ε, in the form of partial differential equations will be established as: [42–46].

$$\frac{\partial}{\partial t}(\rho k)+\frac{\partial}{\partial X_j}(\rho k u_j)=\frac{\partial}{\partial X_j}\left[\left(\mu+\frac{\mu_t}{\sigma_k}\right)\frac{\partial k}{\partial X_j}\right]+G_k+G_b+S_k-Y_M-\rho\varepsilon \quad (1)$$

$$\frac{\partial}{\partial t}(\rho\varepsilon)+\frac{\partial}{\partial X_j}[\rho\varepsilon u_j]=\frac{\partial}{\partial X_j}\left[\left(\mu+\frac{\mu_t}{\sigma_\varepsilon}\right)\frac{\partial \varepsilon}{\partial X_j}\right]+C_{1\varepsilon}\frac{\varepsilon}{k}(G_k+C_{3\varepsilon}G_b)-C_{2\varepsilon}\rho\frac{\varepsilon^2}{k}+S_\varepsilon \quad (2)$$

where $G_k$ and $G_b$ represent the turbulent kinetic energy based on the mean velocity gradient and the turbulent kinetic energy based on buoyancy, respectively. $Y_M$ represents the pulsating expansion in the total dissipation rate in compressible turbulence. $C_{1\varepsilon}$, $C_{2\varepsilon}$, and $C_{3\varepsilon}$ are constants. $\sigma_k$ and $\sigma_\varepsilon$ denote the turbulent Prandtl numbers for $k$ and ε, respectively. $S_k$ and $S_\varepsilon$ are user-defined source terms. ρ and ν are the density and the kinematic viscosity, respectively. The turbulent (or eddy) viscosity, $\mu_t$, can be calculated based on $k$ and $\varepsilon$:

$$\mu_t=\rho C_\mu\frac{k^2}{\varepsilon} \quad (3)$$

where $C_\mu$ is a constant. The model constants are $C_{1\varepsilon}$ = 1.44, $C_{2\varepsilon}$ =1.92, $C_\mu$ =0.09, $\sigma_k$ =1.0, and $\sigma_\varepsilon$ =1.3, respectively.

Since the temperature distribution of the module needs to be obtained, the energy equation is therefore given by:

$$\frac{\partial}{\partial t}\left[\rho\left(e+\frac{\nu^2}{2}\right)\right]+\nabla\cdot\left[\rho\nu\left(h+\frac{\nu^2}{2}\right)\right]=\nabla\cdot\left(k_{eff}\nabla T-\sum_j h_j\vec{J}_j+\bar{\bar{\tau}}_{eff}\cdot\vec{v}\right)+S_h \quad (4)$$

where $k_{eff}$ represents the effective thermal conductivity (= $k + k_t$, where $k_t$ is the turbulent thermal conductivity of the turbulence model), and $\vec{J}_j$ is the diffusion flux of species $j$. The first three terms on the right side of Eq. (4) represent the energy transfer due to conduction, species diffusion, and viscous dissipation, respectively. $S_h$ includes the defined volumetric heat sources and the heat generation rate of the chemical reaction. However, this reaction source is not applicable to the overall enthalpy equation. In Eq.(4), the enthalpy $h$ for an ideal gas is defined as:

$$h = \sum_j Y_j h_j \tag{5}$$

For incompressible materials, $h$ includes the pressure work contribution:

$$h = \sum_j Y_j h_j + \frac{P}{\rho} \tag{6}$$

In Eqs. (5 and 6), $Y_j$ is the mass fraction of species $j$, and $h_j$ is the enthalpy change due to specific heat of species $j$:

$$h_j = \int_{T_{ref}}^{T} c_{p,j}\, dT \tag{7}$$

For the pressure-based solver, $T_{ref}$ is 298.15 K.

The internal energy $e$ for compressible and incompressible materials is uniformly defined as

$$e = h - \frac{p_{op} + p}{\rho} \tag{8}$$

In Eq. (8), $p$ and $p_{op}$ are gauge pressure and working pressure, respectively. To calculate the enthalpy and internal energy of an incompressible ideal gas can use the following general formula:

$$h = C_p T + \frac{P}{\rho} \tag{9}$$

For a liquid coolant model, the k-ε model-based Navier-Stokes equations can be used. There conservation equations for the momentum, continuity, and energy terms are, respectively [47]:

$$\frac{\partial \vec{v}_w}{\partial t} + (\nabla \cdot \vec{v}_w)\vec{v}_w = -\frac{1}{\rho_w}\nabla p + \eta \nabla^2 \vec{v}_w \tag{10}$$

$$\frac{\partial \rho_w}{\partial t} + \nabla(\rho_w \vec{v}_w) = 0 \tag{11}$$

$$\frac{\partial T_w}{\partial t} + (\nabla \cdot \vec{v}_w)\, T_w = \frac{k_w}{\rho_w c_w}\nabla^2 T_w \tag{12}$$

where $\rho_w$, $c_w$, $k_w$, and $\eta$ represent the density, specific heat, thermal conductivity, and kinematic viscosity of coolant (water), respectively. $v_w$, $p$, and $T_w$ are the velocity vector, the static pressure, and the temperature of the coolant (water), respectively.

For the air-cooling part, the three conservation equations are [48]:

$$\frac{d}{dt}(\rho\, v_a) + \nabla \cdot (\rho_a \vec{v}_a) = -\nabla p \tag{13}$$

$$\frac{\partial \rho_a}{\partial t} + \nabla \cdot (\rho_a \vec{v}_a) = 0 \tag{14}$$

$$\rho_a c_{va} \frac{\partial T_a}{\partial t} + \nabla \cdot (\rho_a c_{va}\, \vec{v}_a T_a) = \nabla \cdot (k_a \nabla T_a) \tag{15}$$

where $k_a$, $T_a$, $v_a$, $c_{va}$, and $\rho$ denote the thermal conductivity, temperature, velocity vector, specific heat, and static pressure of air, respectively.

### *3.3. Physical Parameters, and Boundary and Working Conditions in Modeling*

The pack-level BP thermal models consist of a 3-battery-cell BP, four thermally conductive silicone plates, two liquid cooling aluminum plates, and two aluminum shells, referring to Figure 2.

The entire system adopts an incomplete encapsulation structure for air passing through and liquid circulation. The BP shell is constructed from aluminum plates. The BP model created incorporates three square Li-ion phosphate batteries. Liquid cooling plates with identical parameters are positioned both above and below the battery assembly. 2mm-thick thermally conductive silicone plates are inserted between the batteries and between the battery assembly and the liquid cooling plates. Both the liquid cooling plate and the BP casing are crafted from aluminum plates. The aluminum plate casing of the liquid cooling plate measures 2mm in thickness, while the aluminum plate casing of the BP measures 3.85mm in thickness.

The natural air convection between the housing and the surrounding air can be determined by [47]:

$$-K_s\frac{\partial T}{\partial n}=(T_s-T_a)h_{nat} \tag{16}$$

where the convection coefficient of the natural air $h_{nat}$ is $5\,\mathrm{W}/(m^2\cdot K)$. $K_s$ represents the thermal conductivity of the shell, and $T_s$ and $T_a$ represent the shell and ambient temperatures respectively. $n$ indicates the wall normal.

The heat generation rate of Li-ion batteries mainly relies on theoretical calculations. In order to ensure calculation efficiency, reasonable assumptions are made for the physical model in the simulation as follows:

(1) The density, thermal conductivity, and specific heat of each material do not change with temperature and SOC.

(2) The thermal conductivity of battery materials is anisotropic and changes in different directions, while the thermophysical parameters in the same direction are constant.

(3) The heat generation rate of the battery remains unchanged, and the current density is evenly distributed.

(4) Ignore radiation during heat transfer.

(5) The Coolant (water) is considered as an incompressible Newtonian fluid. Since heat conduction plays a major role in the BTMS heat transfer process, its natural convection is ignored.

(6) Based on the principle of simplified model, the battery only retains the structural dimensions and the function of heating part of the battery core by ignoring the details of the positive and negative electrode tabs and busbar.

The specific physical parameters of the BP without a BTMS (only having natural air passive cooling), with a hybrid BTMS (having natural air passive cooling and a water coolant active cooling), and with a composite BTMS (having forced air active cooling and a water coolant active cooling) are listed in Table 1, 2, and 3 [49,50].

**Table 1.** Physical parameters of the BP without BTMS (only natural air passive cooling).

| The Parameter | Value | Units |
|---|---|---|
| | **Air** | |
| Initial temperature | 25.0 | °C |
| Initial flowrate | 0.0 | m/s |
| Density | 1.225 | Kg/m$^3$ |
| Specific heat | 1006 | J/(kg·K) |
| Thermal conductivity | 0.0242 | W/(m·K) |
| Kinematic viscosity | 1.789×10$^{-5}$ | Kg/(m$^1$·s) |
| | **Silicone thermal conductive plate** | |
| Size (between batteries) | 148.3 × 1.5 × 129.8 | mm × mm × mm |
| Size (between battery and liquid cooling plate) | 189.7 × 152 × 2 | mm × mm × mm |
| Density | 1130 | Kg/m |
| Specific heat | 1320 | J/(kg·K) |
| Thermal conductivity | 2.0 | W/(m·K) |
| | **Liquid cooling plate and walls** | |

| | | |
|---|---|---|
| Size of LCP | 162 × 152 × 21 | mm |
| Density (Al) | 2719 | Kg/m$^3$ |
| Specific heat (Al) | 871.0 | J/(kg·K) |
| Thermal conductivity (Al) | 202.4 | W/(m·K) |
| **Heat convection coefficient** | | |
| Wall | 5.0 | W/(m$^2$·K) |
| Thermal pad | 5.0 | W/(m$^2$·K) |

**Table 2.** Physical parameters of the BP with hybrid BTMS (having natural air- and water-cooling).

| The Parameter | Value | Units |
|---|---|---|
| **Water** | | |
| Initial temperature | 25.0 | °C |
| Initial flowrate | 0.5 | m/s |
| Thermal conductivity | 0.6 | W/(m·K) |
| Kinematic viscosity | 0.001003 | m$^2$/s |
| Specific heat | 4182 | J/(kg·K) |
| Size (Between battery and liquid cooling plate) | 189.7 × 152 × 2 | mm × mm × mm |
| Density | 998.2 | Kg/m$^3$ |
| Other component temperature | 25.0 | °C |
| **Changes in coolant (water) conditions** | | |
| Temperature/flowrate/convection coefficient* | 30/0.5/128.5 | °C; m/s; W/(m$^2$·K) |
| Temperature/flowrate/convection coefficient* | 20/0.5/701.9 | °C; m/s; W/(m$^2$·K) |
| Temperature/flowrate/convection coefficient* | 25/0.8/225.9 | °C; m/s; W/(m$^2$·K) |
| Temperature/flowrate/convection coefficient* | 25/1.0/279.4 | °C; m/s; W/(m$^2$·K) |
| **Heat convection coefficient** | | |
| Wall | 5.0 | W/(m$^2$·K) |
| Thermal pad | 5.0 | W/(m$^2$·K) |
| **The properties of natural air, silicone thermal conductive plates, liquid cooling plates, and walls are the same as in Table 1** | | |

* Note: the maximum BP surface heat convection coefficients at a fixed position at the inlet of the liquid-cooling pipe. The effective convective coefficient, $h_{eff}$, regarding the overall cooling effect of the BP surface, can be calculated through the ANSYS® fluent program based on the following equation [46]:.

$$h_{eff} = \frac{q}{T_{wall} - T_{ref}} \tag{17}$$

where $T_{ref}$ and $T_{wall}$ are the reference temperature defined as room temperature of 25°C and the wall temperature, respectively. $q$ is the heat flux.

The selected battery in this case study is EVE LF50F Lithium Energy square lithium iron phosphate battery. The battery has a long cycle life, low battery internal resistance and high discharge rate. It has been widely used in the EV market and industrial energy storage. Table 4 lists the battery's physical parameters [50].

**Table 3.** Physical parameters of the BP with BTMS having forced air and water coolant active cooling.

| The Parameter | Value | Units |
|---|---|---|
| **Water** | | |
| Initial temperature | 25.0 | °C |

| | | |
|---|---|---|
| Initial flowrate | 0.5 | m/s |
| **Air** | | |
| Initial temperature | 25.0 | °C |
| Initial velocity | 1.0 | m/s |
| Density | 1.225 | Kg/m$^3$ |
| Specific heat | 1006 | J/(kg·K) |
| Thermal conductivity | 0.0242 | W/(m·K) |
| Kinematic viscosity | $1.789\times10^{-5}$ | Kg/(m·s) |
| **Changes in air conditions** | | |
| Temperature/flowrate/convection coefficient* | 30/1/20.60 | °C; m/s; W/(m$^2$·K) |
| Temperature/flowrate/convection coefficient* | 20/1/23.78 | °C; m/s; W/(m$^2$·K) |
| Temperature/flowrate/convection coefficient* | 15/1/61.67 | °C; m/s; W/(m$^2$·K) |
| Temperature/flowrate/convection coefficient* | 25/2/17.02 | °C; m/s; W/(m$^2$·K) |
| Temperature/flowrate/convection coefficient* | 25/0.5/13.51 | °C; m/s; W/(m$^2$·K) |
| **The properties of silicone thermal conductive plates, liquid cooling plates, and walls are the same as in Table 1** | | |

* Note: the maximum BP surface heat convection coefficients at a fixed position at the inlet of the air-cooling channel based on the above calculations (referring to Eq.(17)).

**Table 4.** Physical parameters of the Battery LF50F.

| The Parameter | Value | Units |
|---|---|---|
| **Battery** | | |
| Nominal voltage | 3.20 | V |
| Nominal capacity | 50 | Ah |
| Standard cycle (at 25°) | 1500 (0.5C) | |
| Internal resistance (1KHz) | ≤ 2.0 | mΩ |
| Weight | 1035±100 | g |
| Size (height × width × thickness) | 129.8 × 148.3 × 26.7 | mm × mm × mm |
| Distance between the adjacent battery cells | 1.5 | mm × mm × mm |
| Density | 2519 | Kg/m$^3$ |
| Specific heat | 1022.8 | J/(kg·K) |
| Thermal conductivity (x-direction) | 1.062 | W/(m·K) |
| Thermal conductivity (y/z-direction) | 22.45 | W/(m·K) |
| **Discharge** | | |
| Discharge rate (C) | Total time steps | Time step size (s) |
| 0.5 | 3600 | 2 |
| 1.0 | 1800 | 2 |
| 2.0 | 900 | 2 |
| 3.0 | 600 | 2 |

The basis of temperature filed simulation of Li-ion BP is the thermophysical parameters of battery materials. Accurate thermophysical parameters are of great significance to the accuracy of simulation results. In practical applications, accurately obtaining the heat generation rate of the battery during charging and discharging operation is a challenge. There are two ways to solve the problem: experimental measurement and theoretical calculation. This work mainly uses the battery heat generation rate model proposed by Bernardi [51]. The battery heat generation rate is calculated and to be used in the CFD simulations as:

$$q = \frac{I}{V}[(U_0 - U) + T\frac{\partial U_0}{\partial T}] \quad (18)$$

This model divides the battery generated heat into two categories: Joule heat and reversible reaction heat. *I* is the charge and discharge current, which is negative during charging and positive during discharging; V represents the battery volume; $U_0$ and $U$ represent the open circuit voltage and the battery terminal voltage, respectively; $\frac{\partial U_0}{\partial T}$ is the temperature gradient of the open circuit voltage, generally a constant 0.5Mv/K; and $T$ is the battery temperature. Since the internal resistance of the battery $R$ does not change much when the battery is charging or discharging, therefore, in this work, a $R$ value of 2.0 mΩ was selected [50]. Because $U_0$-$U$ = $IR$, then, Eq. (18) can be rewritten as:

$$q = \frac{1}{V}[I^2R - IT\frac{\partial U_0}{\partial T}] \quad (19)$$

Table 5 lists the heat generation rate of a single battery cell at different discharge rates, calculated according to Eq. (18)).

**Table 5.** Heat generation rates of a single battery cell at various discharge rates.

| Discharge rate (C) | 0.5 | 1 | 2 | 3 |
|---|---|---|---|---|
| Volumetric heat source ($W/m^3$) | 2486.1 | 9944.3 | 38777.3 | 89498.8 |
| Operation time (s) | 7200 | 3600 | 1800 | 1200 |

In this study, the BTMS design primarily emphasizes heat dissipation and temperature distributions, i.e., average temperature, maximum temperature, and minimum temperature, in the BP. As a result, water-ethylene glycol, which offers superior thermal insulation but poor thermal conductivity, is not chosen as the coolant. Additionally, since the BP is designed as a non-sealed structure, it does not utilize insulating thermal oil commonly found in immersion cooling systems. Instead, water is selected as the cooling medium. The liquid cooling plate is designed with a multi-channel configuration featuring five water inlets and five water outlets layout above and below the BP, as shown in Figure 2.

This simulation involved the coupled modeling of the heat transfer between fluid and solid. The water coolant flows in the pipeline, and the viscosity model needs to be determined. The flow state is determined according to the Reynolds number *Re*, where $Re < 2300$ is a laminar flow, $Re > 4000$ is a turbulent flow, and *Re* between 2300 and 4000 is a transitional flow. The Reynolds number *Re* is calculated by [52]:

$$Re = \frac{\rho v D}{\mu} \quad (20)$$

where $\mu$, $\rho$, and $v$ are the fluid viscosity coefficient, the fluid density, and the fluid flow rate, respectively. $D$ is the flow path equivalent diameter.

The liquid cooling plates designed in this work are rectangular plates, and the shear stress is unevenly distributed around the interface. Therefore, the equivalent diameter of the cooling plate interface can be converted as [53]

$$D = \frac{4A_c}{P_w} \quad (21)$$

where $A_c$ and $P_w$ are the cross-sectional area and the wetting perimeter of the liquid cooling plate, respectively. The maximum flow rate of common vehicle water pumps on the market is 10L/min-40L/min [54,55]. In this model, as shown in Figure 2, if using a 120L/min automotive water pump, the maximum coolant velocity is 1.656 m/s, so it is reasonable to select a flow rate of 0.5 m/s at the

doi:10.20944/preprints202501.0859.v1

coolant (water) inlet of the cooling plate. The calculated Reynolds number *Re* is ranging from 3083 to7706 in this work. The model is a turbulence model.

In this study, the thermal conduction within the silicone thermal conductive plate and the liquid cooling plate (the same as the silicone thermal conductive plate) were considered, which is calculated as [47]

$$\nabla \cdot (k\nabla T) = \rho c \frac{\partial T}{\partial t} \tag{22}$$

where $\rho$, $c$, and $k$ represent the density, the specific heat, and the thermal conductivity of the silicone plate, respectively.

### *3.4. Mesh Convergence Study*

In solid mechanics or CFD simulations based on finite element analysis, finer meshes usually produce solutions with higher accuracy. However, as the meshes become finer, the computation time increases. Therefore, it needs to determine a proper mesh size (or total element number) with a satisfactory balance between accuracy and computational resources. One common approach is to perform a mesh independent study or called mesh convergence study. This process includes the following basic steps:

- Create a mesh using a minimum or reasonable number of elements and reasonable element size and analyze a specific convergence output variable or variables, such as maximum displacement of the problem in the solid mechanics problems or maximum, minimum, or average temperature in the thermal problem in this study.
- Recreate the mesh with a denser element distribution or finer elements, re-analyze the specific output variable/s and compare the results with those of the previous solutions.
- Keep increasing the mesh density and re-analyzing the modeling results until the specific output variable/s from the modeling result converge satisfactorily.

In this study, a poly-hexagonal core shape for the mesh is available in ANSYS® Fluent and was adopted in both the prismatic battery and coolant flow systems, which is better suited for accommodating prismatic and vertical boundaries, and it exhibits greater sensitivity to local changes. In order to conduct the mesh convergence study, firstly, it was decided to use the designed battery model for mesh independence study, i.e., a pack-level BP model with 3-battery cells with a composite BTMS (under forced air: a flowrate of 1m/s and an initial temperature of 25°C; and water cooling: a velocity of 0.5 m/s and an initial temperature of 25°C) was meshed and simulated using different numbers of elements or different element sizes. Figure 3 shows the curves of the output variables, such as average, maximum, and minimum temperatures in the BPs, varying with the number of elements (1.85, 4.44, 9.42, and 13.67 million) under discharge rate of 3C at operation time of 1200s. Figure 4 shows the bar chart plot of the average, maximum, and minimum temperatures of the different battery cells (cell 1, cell2, and cell 3) in the BPs, varying with the numbers of elements under discharge rate of 3C at operation time of 1200s. Figure 5 shows the relative percent errors of the simulated average, maximum, and minimum temperatures in the BPs, vary with the numbers of elements under discharge rate of 3C at operation time of 1200s. When the number of element exceeds 4.44 million, the relative errors of the specific output temperatures of the BPs are less than 0.08%. Therefore, the pack-level BP with a composite BTMS model with 4.44 million elements was adopted which has sufficient accuracy for the simulations. The 3D view of the meshed BP with a composite BTMS model with 4.44 million elements is shown in Figure 6.

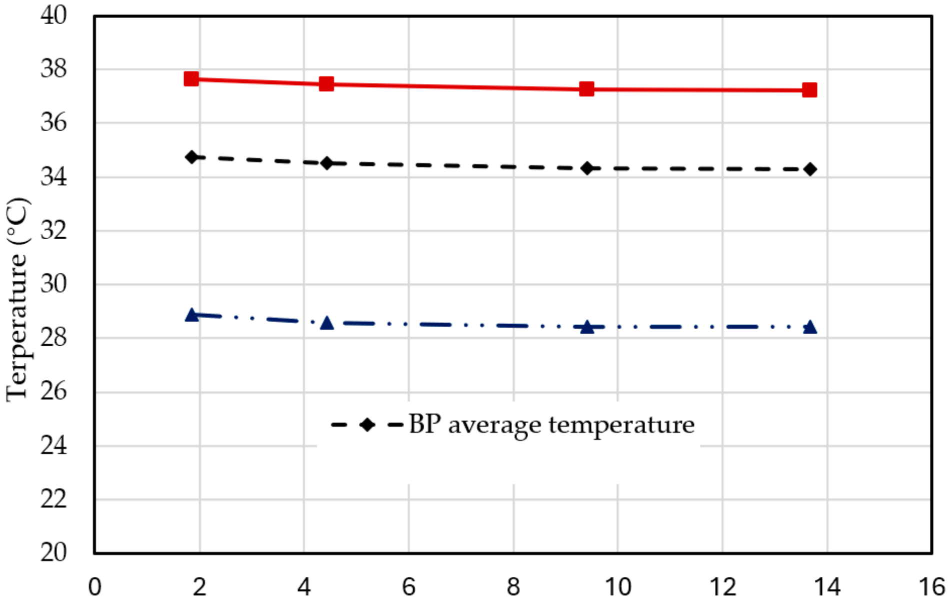

**Figure 3.** Mesh convergence study on temperatures in a 3-battery-cell BP with a composite BTMS (forced air: a flowrate of 1m/s and an initial temperature of 25°C; and water cooling: a flowrate of 0.5 m/s and an initial temperature of 25°C), vs. number of elements at a discharge rate of 3C and operation time of 1200s.

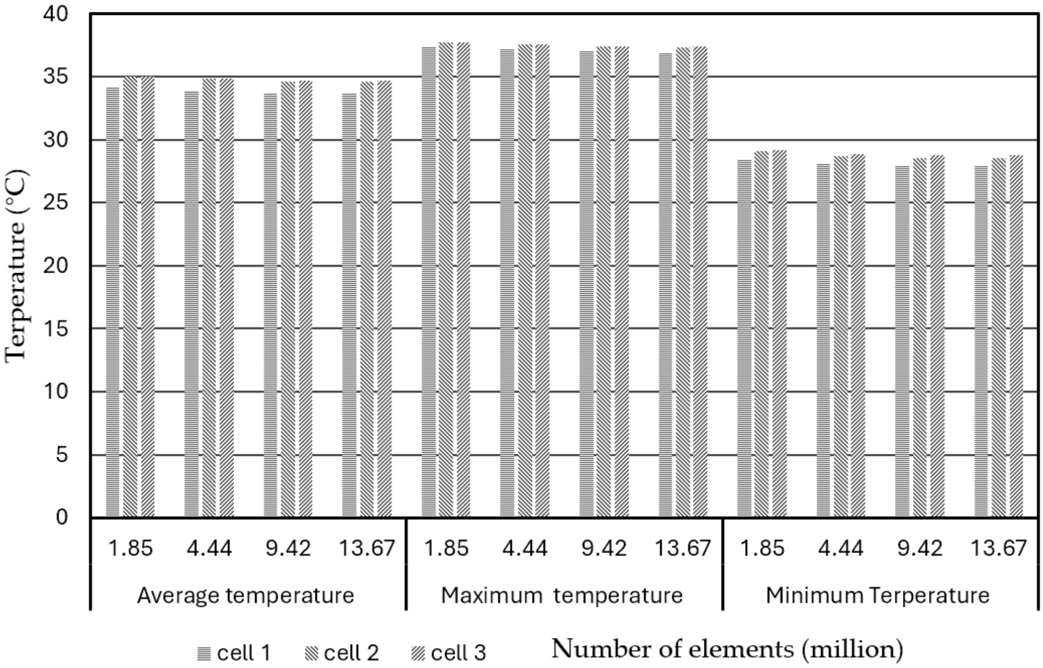

**Figure 4.** Mesh convergence study on temperatures in different battery cells of a 3-battery-cell BP with a composite BTMS (forced air: a flowrate of 1m/s and an initial temperature of 25°C, and water cooling: a flowrate of 0.5 m/s and an initial temperature of 25°C), vs. number of elements at a discharge rate of 3C and operation time of 1200s.

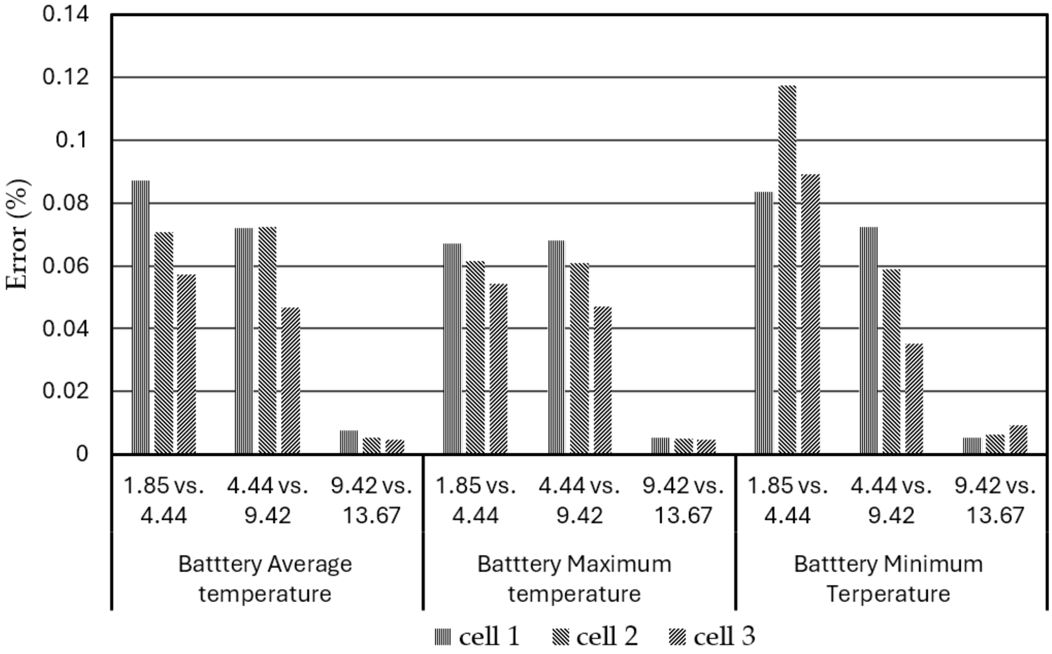

**Figure 5.** Mesh convergence study on relative percentage error in temperatures in different battery cells of a 3-battery-cell BP with a composite BTMS (forced air: a flowrate of 1m/s and an initial temperature of 25°C; and water cooling: a flowrate of 0.5 m/s and an initial temperature of 25°C), vs. number of elements at a discharge rate of 3C and operation time of 1200s.

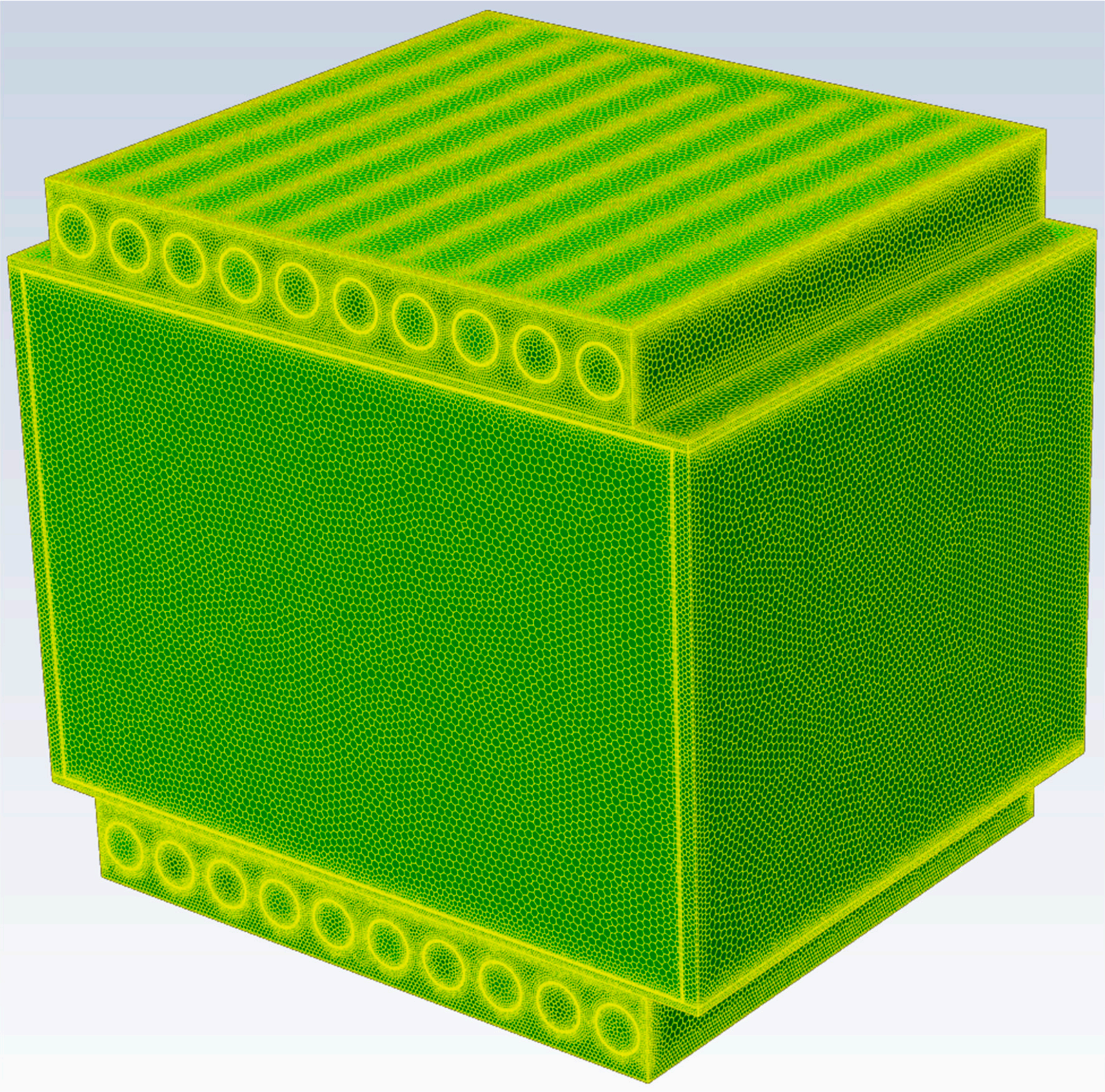

**Figure 6.** 3D view of the 3-battery-cell BP model meshed with 4.44 million elements.

## 4. Results and Discussion

When an EV maintains a constant speed, the discharge rate of its individual battery typically remains stable, resulting in a consistent temperature change within the battery. However, various factors, such as road conditions, traffic congestion, and individual driving habits, can lead to irregular driving patterns. During scenarios like ascending hills or rapid acceleration, the battery's discharge rate experiences significant fluctuations over short durations, consequently affecting its temperature dynamics. Therefore, this study adopts a three-battery-cell BP models to simulate and discuss several cases under various boundary conditions and working parameters, such as cooling methods, discharge rates, operation times, coolant flowrates and initial temperatures, forced air flowrates and initial air temperatures. The simulation cases include: (1) the BP thermal performance without a BTMS (natural air convection cooling only); (2) effect of coolant (water) in a hybrid BTMS on the BP thermal performance; (3) effect of discharge rate on the BP thermal performance; and (4) effect of forced air cooling in a composite BTMS on the BP thermal performance. (5) Finally, the thermal performance of the three-battery-cell BP used as a battery module (BM) installed in a larger BP system was evaluated based on CFD, considering the different BM positions located in the larger BP system (at the corner and at the middle edge of the BP or independently placed).

### *4.1. BP Thermal Performance without BTMS*

doi:10.20944/preprints202501.0859.v1

In this case, the BP consists of three battery cells in each group without a BTMS (heat exchanging with the surrounding environment through natural air convection – passive cooling), and the temperature distributions in the BP under an extreme discharge rate of 3C were simulated and analyzed. According to Table 5, the discharge operation time was taken up to 1200 seconds, and the initial temperature in the model was set to 25°C. The thermal properties of the model refer to Table 1. Figure 7 shows the surface temperature distribution of the BP without a BTMS at a discharge rate of 3C and operation time of 1200s. Usually, due to the worst heat dissipation effect, the maximum temperature appears in the middle of the BP, and the minimum temperature appears at the corners of the BP. The average, maximum, and minimum temperatures when viewed from the front, rear, side, and top are quite close and symmetric. The minimum and maximum temperature are 59.8°C and 63.6°C, respectively, much higher than the ROTR (+20°C ~+35°C). The maximum temperature difference is less than 4°C, indicating that under this natural air passive cooling condition, the heat dissipation capability is not effective.

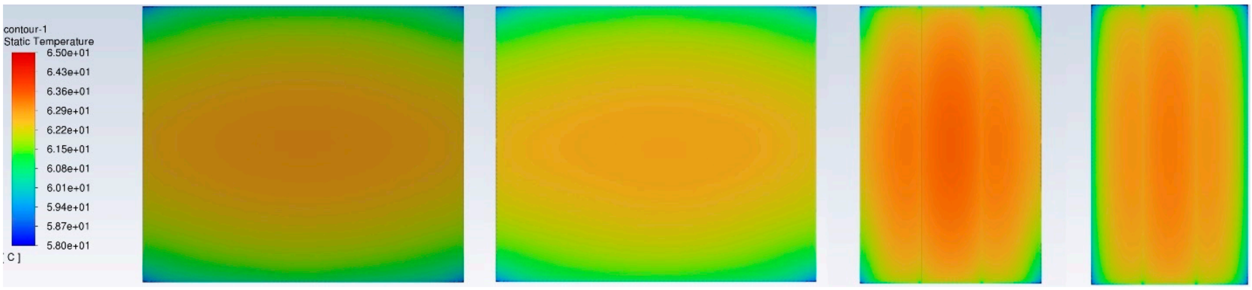

**Figure 7.** Temperature distribution in a three-battery-cell BP surface without a BTMS (natural air convection only) at a discharge rate of 3C and operation time of 1200s (from left to right: front view, rear view, side view, and top view).

### *4.2. Effect of a Hybrid BTMS (water cooling) on BP Thermal Performance*

In this case, the BP model is the same as adopted in Subsection 4.1. For comparison, adding a BP model with a hybrid BTMS, i.e., the natural air convection plus water coolant – active cooling with an initial water flowrate of 0.5m/s and an initial temperature of 25°C. The temperature distributions in the BP under an extreme discharge rate of 3C were simulated and analyzed. The thermal properties of the model are referred to Table 1 and Table 2. According to Table 5, the discharge operation time was taken up to 1200 seconds, and the model's initial temperature was set to 25°C, and other conditions remain unchanged. Therefore, the effect of the hybrid BTMS with defined conditions on the BP thermal performance was simulated and evaluated. Figure 8 shows the temperature distribution in the BP with a hybrid BTMS at a discharge rate of 3C and operation time of 1200s. The maximum temperature rises to about 38.7°C, much lower than the case without a BTMS (24.9°C lower), and slightly above the ROTR (+20°C ~+35°C).

Figure 9 compares the changes in the average, maximum, and minimum temperatures in the BPs without a BTMS or with a hybrid BTMS varying with operation time under a discharge rate. For the BP without a BTMS, the temperatures continuously and rapidly rise with operation time. However, for the BP with additional water-cooling BTMS, the temperatures rise much slower and tend to converge (stable) at a certain value. After installing the liquid (water)-cooling BTMS, the internal temperatures of the BP can be well controlled between 30°C and 40°C. The minimum, maximum, and average temperatures in the BP converge after 1200 seconds of operation time to stable values of 29.64°C, 38.66°C, and 36.02°C, respectively, and they are significantly reduced by 29.67°C, 24.73°C, and 28.89°C, respectively, compared to the BP without a BTMS, and slightly over the recommended temperature range of +20°C ~+35°C.

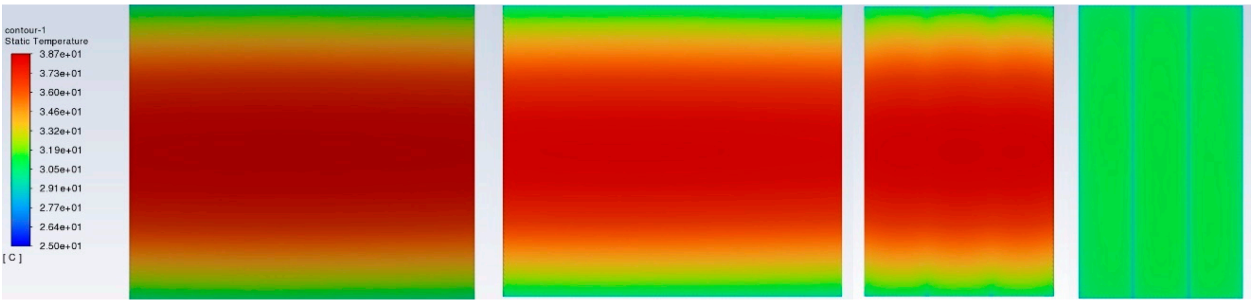

**Figure 8.** Temperature distribution in a BP surface with a hybrid BTMS at a discharge rate of 3C and operation time of 1200s (from left to right: front view, rear view, side view, and top view).

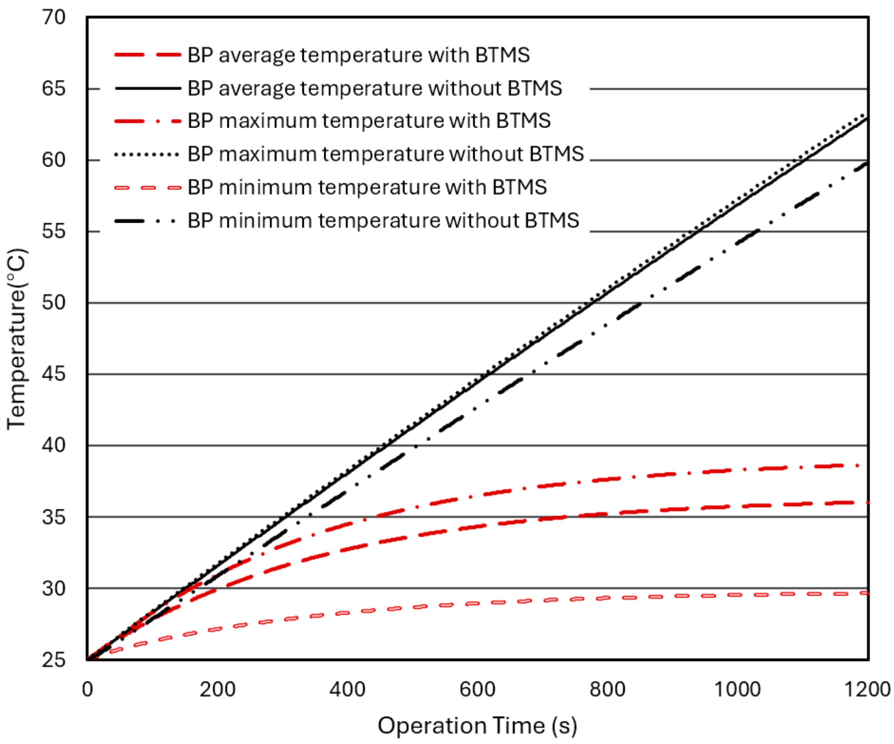

**Figure 9.** Temperature changes in the BPs without a BTMS or with a hybrid BTMS varying with operation time at a discharge rate of 3C.

### *4.3. Effect of Discharge Rate on BP Thermal Performance*

The BP models and conditions are the same as those adopted in Subsection 4.1. Figure 10 shows the effect of the discharge rate (0.5C, 1C, 2C, and 3C) on the average, maximum, and minimum temperatures in the three-battery-cell BPs without a BTMS (natural air convection only). The operation times are calculated according to the discharge rate as shown in Table 5. The initial temperature for the simulations was set to 25°C. As can be seen from Fig. 10, the temperature differences in different battery cells are very close. The higher the discharge rate, the more heat is generated in each cell, and the higher the temperature rises in each cell. When the discharge rate is 3C, the average, maximum and minimum temperatures rise to around 60°C, much higher than the ROTR. Even when the discharge rates are lower than 2C, the temperature of the BP is still higher than that of ROTR.

Figure 11 shows the effect of the discharge rates on the maximum temperature difference in BPs without a BTMS (natural air convection only) or with a hybrid BTMS (water cooling combined with natural air convection) over operation time. The maximum temperature differences in BPs with a hybrid BTMS under different discharge rates are obvious, and the maximum value appears in the BP model with a discharge rate of 3C, reaching 9.0°C. The liquid (water) cooling plates are installed on the upper and lower sides of the batteries, forcing the coolant to dissipate heat to the surrounding area, causing the temperature in the BP to drop significantly, and there is a significant temperature difference between the upper and lower parts of the battery cell compared and the central area.

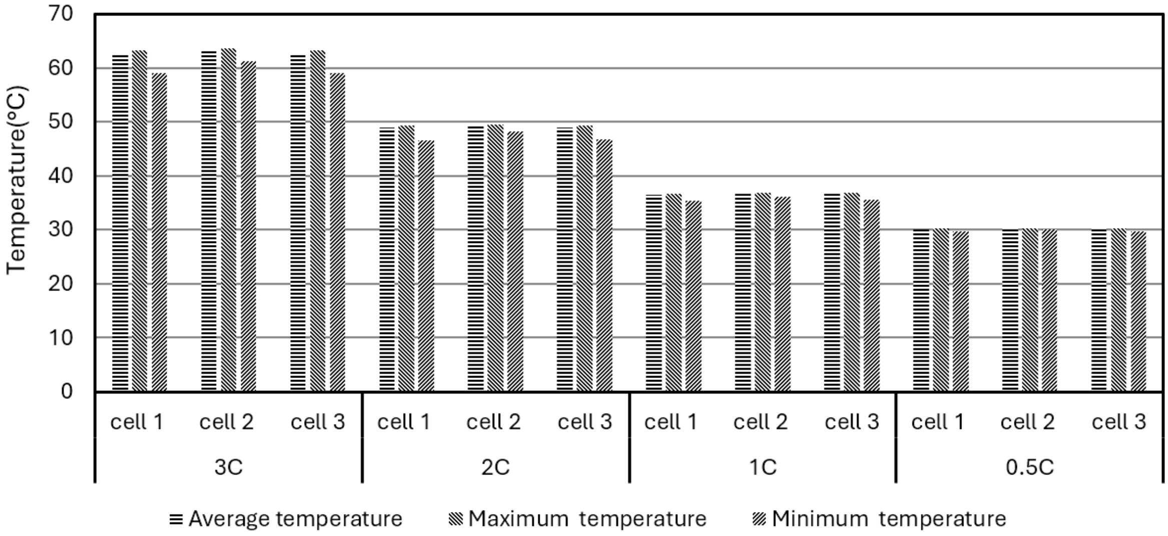

**Figure 10.** Temperatures vs. discharge rate (0.5C, 1C, 2C, and 3C) for a three-battery-cell BP (cell 1, cell 2, and cell 3) without a BTMS (at operation times indicated as in Table 5 corresponding to the discharge rate).

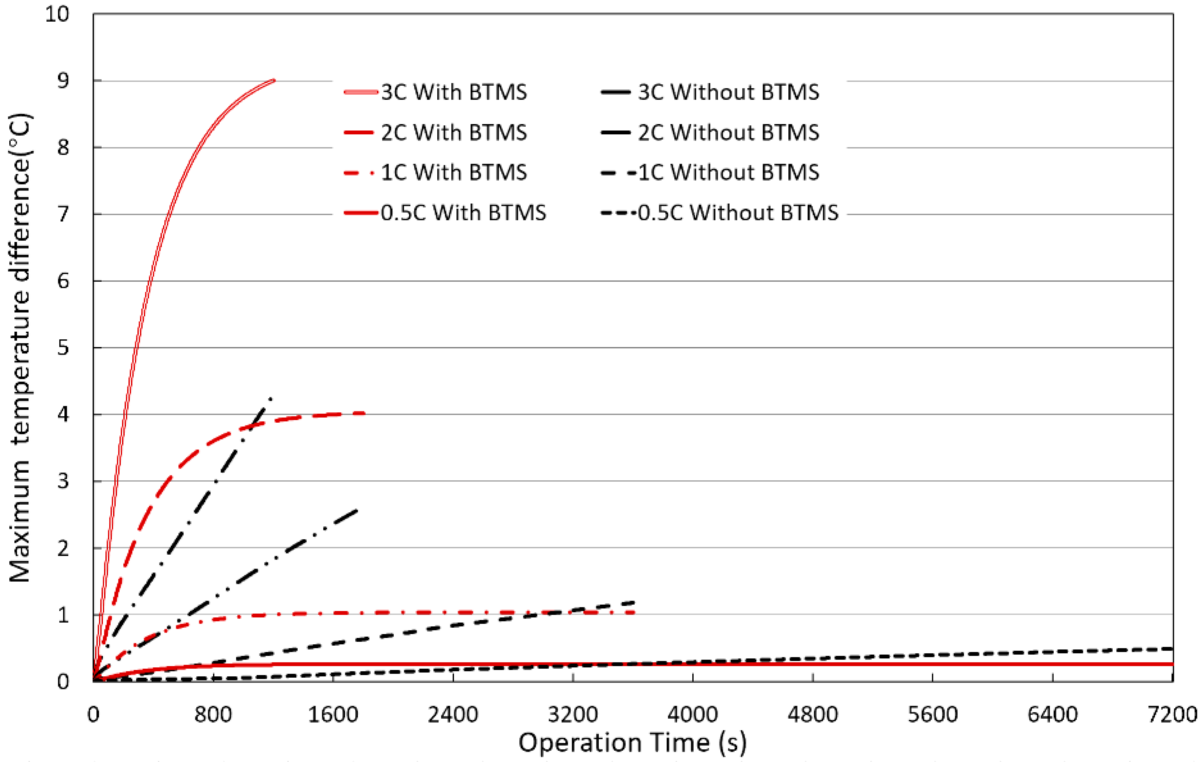

**Figure 11.** Maximum temperature difference vs. operation time at different discharge rates for a three-battery-cell BP with a hybrid BTMS (water cooling and natural air convection) or without a BTMS (natural air convection only).

### *4.4. Effects of Water Coolant Flowrate and Initial Temperature on BP Thermal Performance*

In this case, the BP is still three battery cells per group, the BP model and conditions are the same as in Subsection 4.2. The BPs used a hybrid BTMS and different water coolant flowrates (0.5 m/s, 0.8m/s, and 1.0 m/s) and different initial temperatures (20°C and 30°C) were adopted for simulations. All simulations were carried out at a discharge rate of 3C. Figure 12 shows the effects of water coolant flowrate and initial temperature on the maximum BP temperature. As can be seen, when the initial coolant temperature is 25°C, the maximum temperature curves are almost the same when flowrates are 0.8 m/s and 1.0 m/s, respectively. Even at a flowrate of 0.5 m/s, the curve differs slightly from these two curves, indicating that the water coolant flow rate has less influence on the maximum BP temperature. The coolant initial temperature has a much greater effect on the maximum temperature changes. Figure 13 shows the effects of the water coolant flow rate and the initial temperature on the average temperature in the BPs. The simulated effects of the coolant flow rate and the initial temperature on the average BP temperature are similar to the effects on the maximum BP temperature (as Fig. 12). Figures 12 and 13 show that when the flow rate increases from 0.5 m/s/ to 0.8 m/s, the maximum temperature and average temperature decrease by 1.3°C and 1.5°C, respectively. Further increasing the flow rate to 1 m/s, no significant changes were found, indicating that the cooling effect was not significantly improved. Choosing a coolant initial temperature of 30°C (typical summer conditions), the maximum and average temperatures will rise by 3.3°C and 2.6°C, respectively. While lowering the coolant initial temperature to 20°C significantly lowers the maximum and average temperatures by 5.5°C and 5.7°C, respectively.

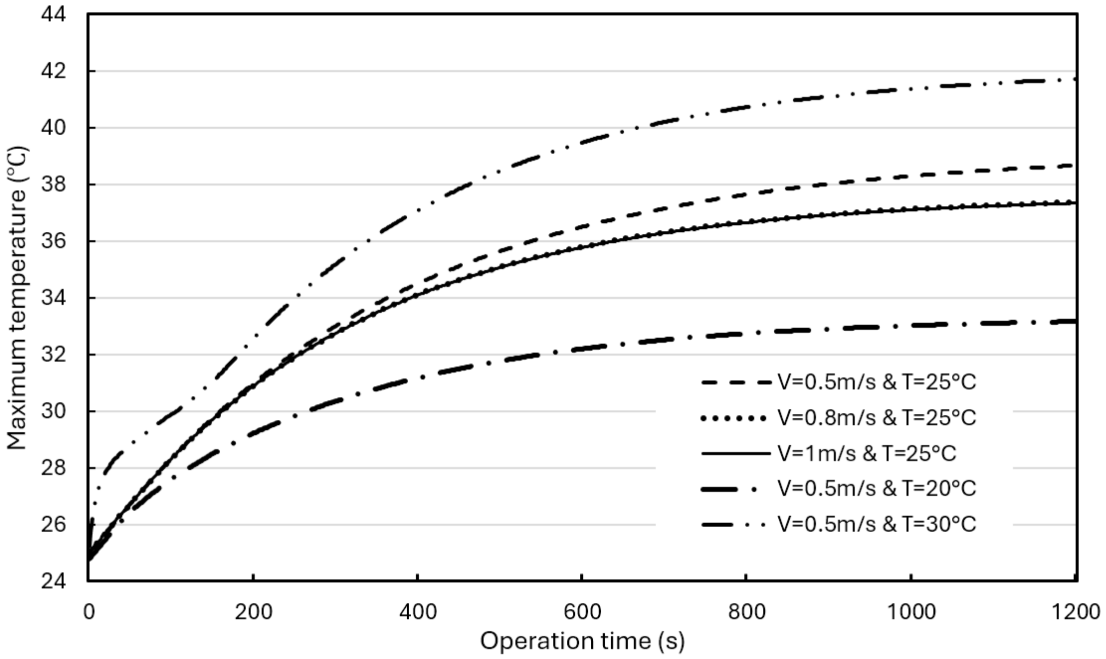

**Figure 12.** Maximum temperature in the BPs vs. operation time at different water coolant flow rates and initial temperatures with hybrid BTMS (water cooling and natural air convection).

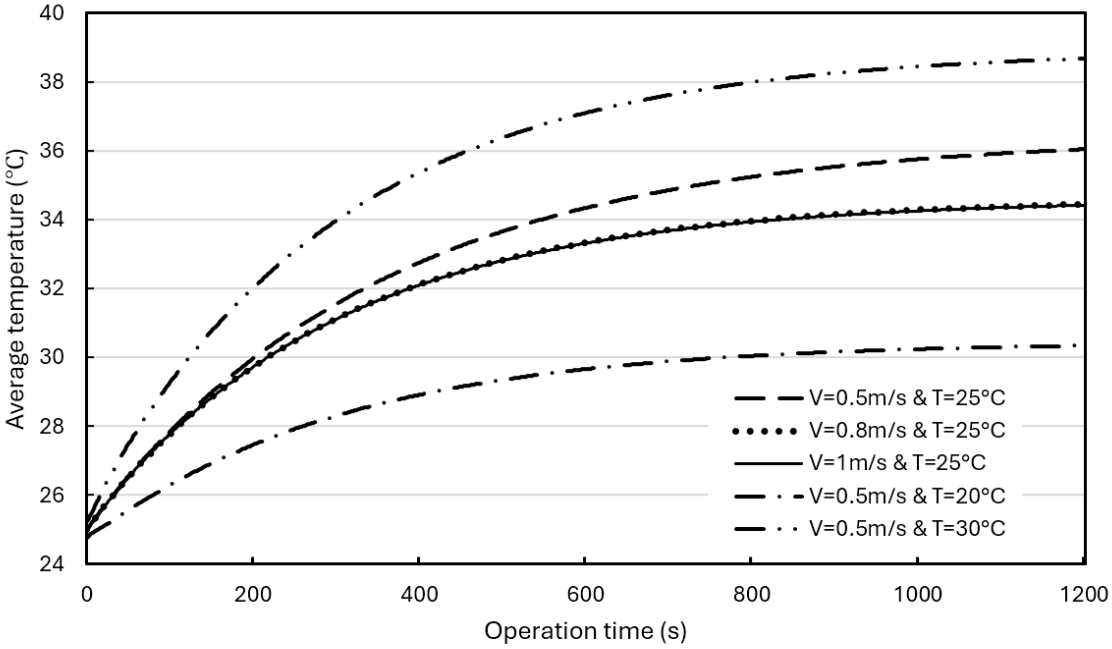

**Figure 13.** Average temperature in the BPs vs. operation time at different water coolant flow rates and initial temperatures with a hybrid BTMS (water cooling and natural air convection).

Figure 14 shows the effects of the water coolant flow rate and initial temperature on the maximum BP temperature difference. Although adjusting the water coolant flow rate and initial temperature will produce different effects, it can be seen that at the beginning of the operation time, due to the coolant initial temperature difference between the BP initial temperature and the coolant initial temperature, the coolant initial temperature has a greater impact on the maximum BP temperature difference. However, after about 1000 seconds, the maximum temperature differences under different operating conditions approach to a similar value of about 9°C, and these differences are negligible, indicating that enhancing the cooling capacity of the water coolant cannot significantly improve the uniformity of the temperature distribution in the BPs, especially on the battery surface. When the coolant initial temperature is 30°C, heat accumulation causes the BP temperature difference to increase rapidly. Similarly, when the coolant initial temperature is 20°C, heat accumulation also occurs, but due to the lower initial temperature, the maximum BP temperature difference increases rapidly and gradually approaches about 9°C. Therefore, lowering the coolant initial temperature is conducive to lowering the BP temperature, and temperature difference in the BP eventually will be the same after a certain operation time.

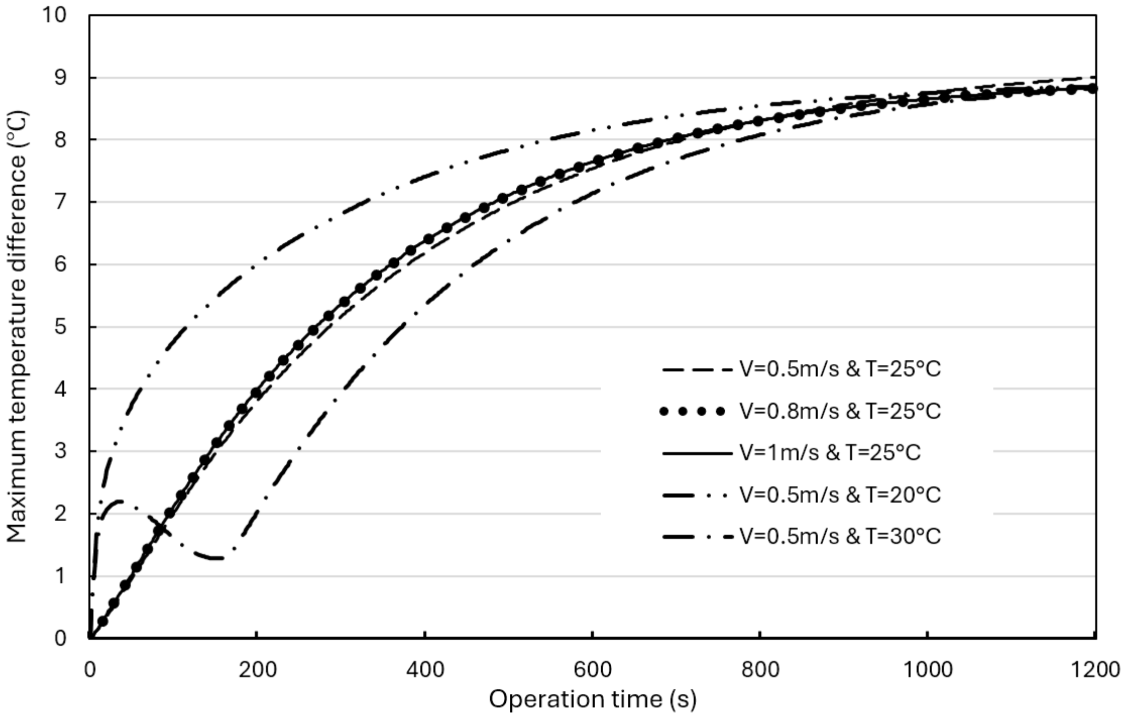

**Figure 14.** Maximum temperature difference in the BPs vs. operation time at different water coolant flow rates and initial temperatures with a hybrid BTMS (water cooling and natural air convection).

### *4.5. Effect of Composite BTMS (forced air cooling combining with water cooling) on BP Thermal Performance*

In the previous subsections, it was concluded that for the designed three-battery-cell BPs, if the BP without a BTMS (natural air convection only), the temperature distribution in the BP will be much higher than the ROTR (+20°C ~+35°C). When the BP is equipped with a hybrid BTMS (adding water coolant cooling to the natural air convection), the water coolant cooling system can effectively enhance the cooling capacity, especially by lowering the coolant initial temperature. However, the maximum temperature in the BP is slightly above the upper bound of the ROTR. In addition, keeping the coolant initial temperature below room temperature consumes a considerable amount of energy, which is not conducive to the efficiency and environmental requirements of the EVs. Therefore, further improvement/design of the current hybrid BTMS was considered. In this case, a composite BTMS (a cooling system combining forced air cooling with water coolant cooling) was designed, since the forced air-cooling system has low cost and the simpler structure (it can be integrated with the vehicle air conditioning system to adjust the BP thermal performance by adjusting fan airflow rate and initial temperature according to the vehicle operating conditions, as shown in Figure 2. The initial conditions of this case were set at an airflow rate of 1 m/s and the initial temperature of 25°C. Figure 15 shows the temperature changes in BP with operation time using a hybrid BTMS or using a composite BTMS at a discharge rate of 3C.

As can be seen, compared with BP using a hybrid BTMS, the composite BTMS can lower the maximum temperature and average temperature in the BPs by 1.2°C and 1.5°C, respectively. However, both BTMSs can stably maintain the BP temperature below 40°C and suitable for high discharge rate conditions.

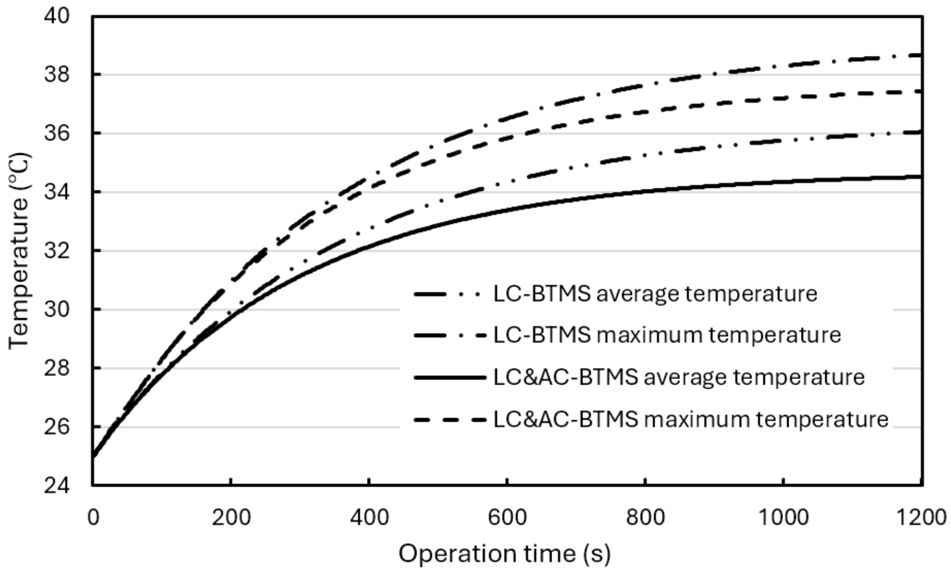

**Figure 15.** Temperatures in BPs vs. operation time with a hybrid BTMS (LC-BTMS) or a composite BTMS (LC&AC BTMS) at a discharge rate of 3C.

In addition, simulations were performed for different airflow rates (0.5 m/s, 1.0 m/s, and 2.0 m/s) and different air initial temperatures (15°C, 20°C, 25°C, and 30°C) for further evaluation. Figure 16 shows the effects of airflow rate and initial temperature on the average temperature in BP with a composite BTMS. At the same airflow rate (1 m/s), adjusting the air initial temperature from 30°C to 15°C, resulting in a 5.1°C drop in the average temperature in the BP at the operation time of 1200s. At the same initial air temperature (25°C), adjusting the airflow rate from 0.5 m/s to 2 m/s did not induce a significant drop in the average BP temperature at the operation time of 1200s (less than 1°C). The temperature curves in the BPs tend to be stable after the operation time of 1200s, and the average BP temperature range with a composite BTMS can be well controlled within the ROTR regardless of the forced airflow rate used in the composite BTMS, even though its maximum temperature is slightly higher than 35°C (around 37.4°C).

During daily use, EV batteries typically discharge at a higher rate for a shorter period. Even a brief discharge of 1C or 2C can significantly increase power output and acceleration. However, frequent high discharge rates can quickly deplete the SOC, especially when accelerating quickly or climbing steep hills, adversely affecting the battery's chemistry, reducing its energy storage capacity and potentially causing long-term performance issues. To mitigate these effects, EV battery management systems typically maintain discharge rates between 0.2C and 0.5C to balance performance, battery life, and safety. Even with DC ultra-fast (150kW) charging, such as the Tesla Model S, the maximum C rate per hour is less than 3C, and this discharge rate is only maintained during the first 15 minutes of charging [56]. Therefore, the 3C discharge rates adopted in these simulations reflect extreme discharge conditions.

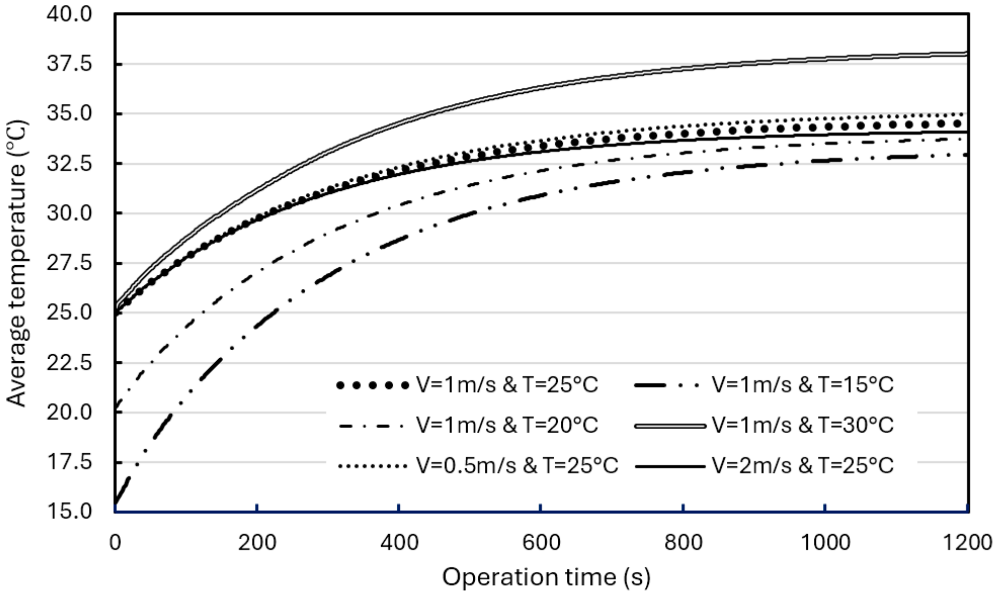

Figure 16. Average temperature in the BPs vs. operation time with a composite BTMS at discharge rate of 3C under different air conditions.

Figure 17 shows the effects of air flowrate and initial temperature on the maximum BP temperature. When the air flows 1 m/s, the initial air temperature has a significant impact on the maximum BP temperature. Lowering the initial temperature from 30°C to 15°C resulted in a 1.7°C drop in the maximum temperature in the BP. However, the inlet airflow rate has a smaller effect on the maximum BP temperature.

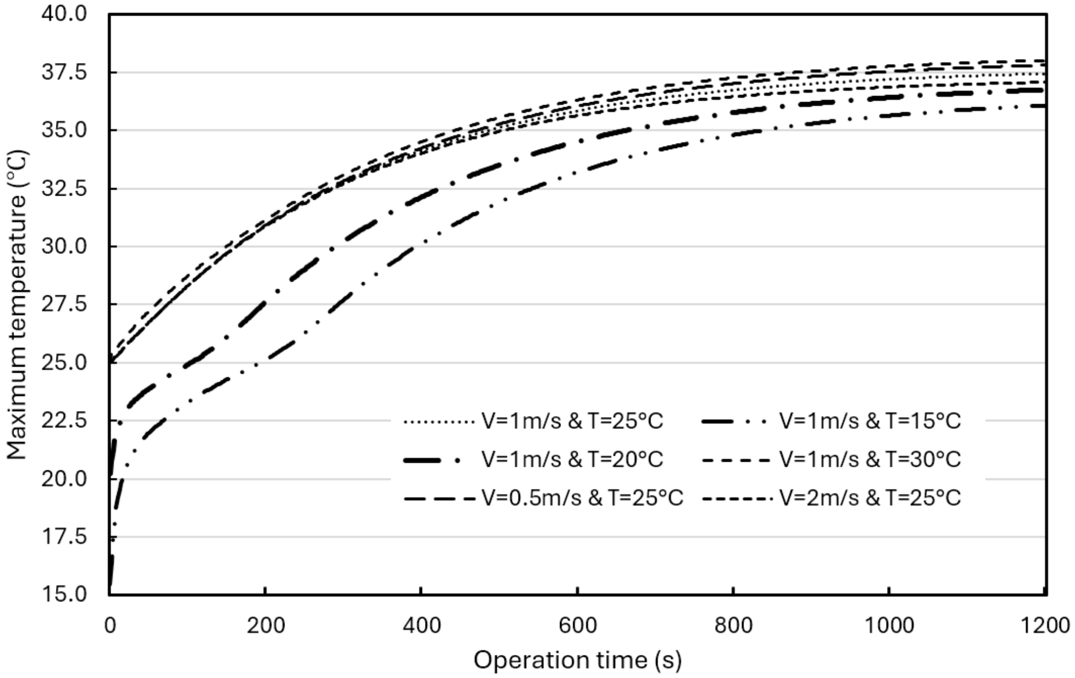

**Figure 17.** Maximum temperatures vs. operation time in BPs with a composite BTMS at discharge rate of 3C under different air conditions.

### *4.6. Summarizing Thermal Performance Comparison of Different BTMS Designs*

So far, the thermal performances of the three-battery-cell BP designed with different cooling systems, such as without a BTMS (natural air convection only), a hybrid BTMS (water coolant cooling with natural air convection), and a composite BTMS (water coolant cooling with forced air cooling), have been simulated and analyzed based on CFD modeling. These thermal performances are summarized and compared in this subsection for conclusive study, as shown in Figure 18.

Figure 18 (a) shows the comparison of the average temperature in the different cells in the BP with the default hybrid BTMS (water coolant temperature of 25°C and flow rate of 0.5 m/s) and the optimal hybrid BTMS (water coolant temperature of 15°C and flow rate of 0.5 m/s). As shown in the figure, the liquid cooling effect is relatively uniform, and the temperatures of the three cells are quite similar. In the case of default hybrid BTMS, the temperatures in the three different cells are almost the same high. In the case of optimal hybrid BTMS, the small rise in temperature for cell 2 is positioned between cell 1 and cell 3, and consistently higher than that of cell 1 primarily because it is affected by heat generation during operation time and heat transfer from both cell 1 and cell 3. As for the small, elevated temperature in cell 3, there are two reasons: first, the coolant absorbs heat from both cell 1 and cell 2 as it flows through cell 3; second, the U-shaped design of the cooling pipes causes the coolant to undergo a 180° turn above the cell 3. When the coolant flows at the U-bend, due to inertia and curvature, the fluid on the outer side accelerates, while the fluid on the inner side decelerates, potentially leading to backflow or stagnation areas. This phenomenon can result in vortices, local stagnation, or reduced flow rates, referred to as fluid stagnation or recirculation. Ultimately, the decrease in flow rate may create a dead zone, thereby reducing the heat dissipation capability. There is a small drop in temperature for cell 1 due to the water coolant pipe is placed over cell 1 and having a better cooling effect on it.

Figure 18(b) shows the comparison of the average temperature in the different cells in the BP with the default composite BTMS (air flowrate of 1 m/s and initial temperature of 25°C) and the optimal composite BTMS (air flowrate of 1 m/s and initial temperature of 15°C). In this case, cell 2 experiences a noticeable temperature rise compared to cell 1 due to its reduced exposure to airflow and the heat transfers from cell 1 and cell 3, positioned at the edge, has the highest temperature due to limited airflow and heat transfer from cell 2. Optimizing the air-cooling parameters can enhance the overall cooling effect of the BTMS but increased the temperature differences between the cells. However, these temperature differences remain within an acceptable range.

Figure 18(c) shows the comparison of the average temperature in the different cells and in the different positions of the BP under the default composite BTMS (air flowrate of 1 m/s and temperature of 25°C). It can be seen a minimal variation in temperature based on the battery position. The differences were so small that they do not show clearly in the comparative figure.

In Figure 18(b) and (c), the temperature difference in the difference cells arise also from the effects of air cooling. Cell 1 is positioned at the windward side of the intake, giving it the largest cooling area. In contrast, cell 2 is subject to heat transfer from both cell 1 and cell 3, resulting in a higher temperature. The temperature arises in cell 3 mainly due to the designed liquid flow in the cooling pipes and its position in the downwind side of the forced air-cooling channel, where airflow carries away heat from cell 1 and cell2, thus reducing its cooling effectiveness. Moreover, the wind exposure areas for cell 2 and cell 3 are roughly the same, leading to their temperatures being significantly higher than that of cell 1, while cell 3 is slightly warmer than cell 2.

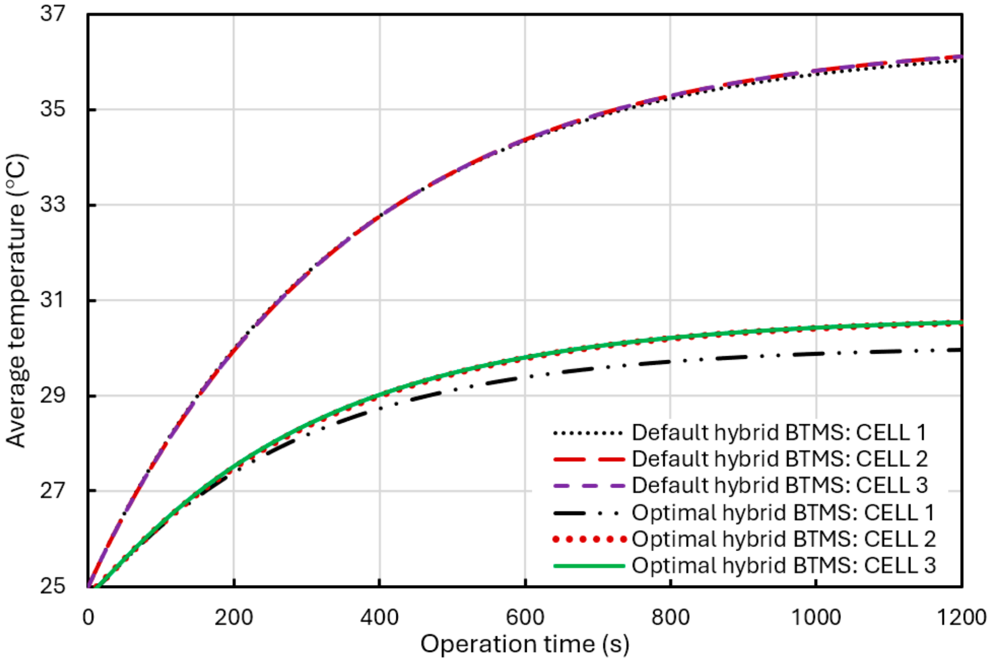
37
35
33
31
29
27
25
Average temperature (°C)
0
200
400
600
800
1000
1200
Operation time (s)
Default hybrid BTMS: CELL 1
Default hybrid BTMS: CELL 2
Default hybrid BTMS: CELL 3
Optimal hybrid BTMS: CELL 1
Optimal hybrid BTMS: CELL 2
Optimal hybrid BTMS: CELL 3

(a)

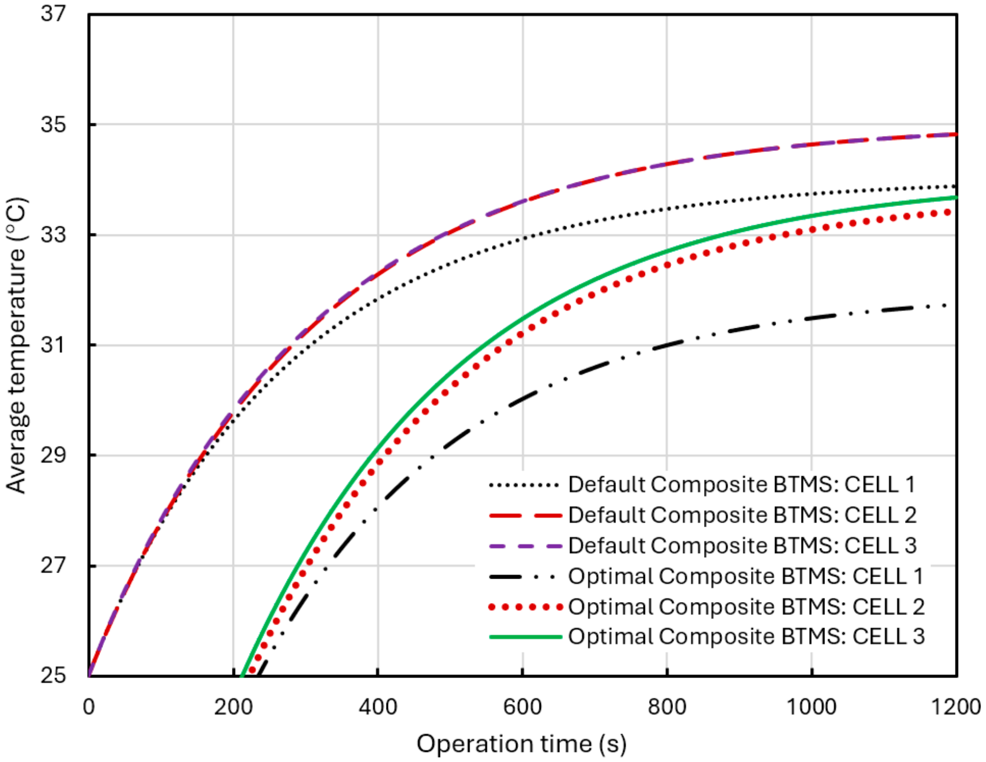
37
35
33
31
29
27
25
Average temperature (°C)
0
200
400
600
800
1000
1200
Operation time (s)
Default Composite BTMS: CELL 1
Default Composite BTMS: CELL 2
Default Composite BTMS: CELL 3
Optimal Composite BTMS: CELL 1
Optimal Composite BTMS: CELL 2
Optimal Composite BTMS: CELL 3

(b)

doi:10.20944/preprints202501.0859.v1

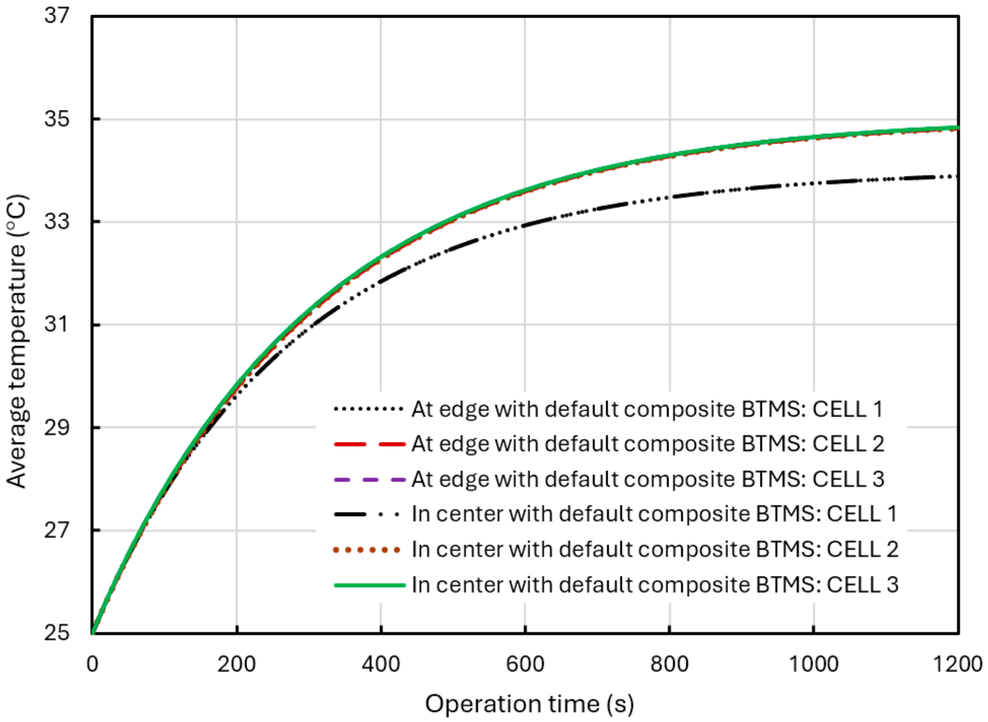

(c)

**Figure 18.** Comparison of thermal performances of the three-battery-cell BP with different cooling systems of different positions: (a) default hybrid BTMS and optimal hybrid BTMS, (b) default composite BTMS and optimal composite BTMS, and (c) at edge or in center of the BP with default composite BTMS.

## 5. Conclusions

In this work, the thermal performances of the three-battery-cell BPs under various operational or environmental conditions were simulated and analyzed, based on the fluid mechanics standard k-ε model and computational fluid dynamics. The following key conclusions have been drawn:

(1) For the BP without a BTMS (natural air convection cooling only), the temperature in the BP rises rapidly and continuously to above the recommended operation temperature range (+20°C~+35°C) under the extreme discharge rate of 3C and even if the discharge rate of 2C.

(2) For the BP with a hybrid BTMS (water coolant cooling plus natural air cooling), the temperature in the BP rises much slower and tends to reach converging values after certain operation time (after 1000s). The temperature at the steady-state is slightly above the recommended operation temperature range even under the discharge rate of 3C. Lowering the coolant (water) initial temperature can effectively lower the temperature in the BP, but the water flowrate can’t.

(3) For the BP with a composite BTMS (water coolant cooling plus forced air cooling), the temperature in the BP rises much slower and tends to reach converging values after certain operation time (after 1000s). The temperature at the steady-state is within the recommended operation temperature range even under the discharge rate of 3C. Lowering the coolant initial temperature and air initial temperature can effectively lower the temperature in the BP, but the coolant flowrate and the air flowrate can’t.

(4) Therefore, a hybrid BTMS can meet the cooling needs in the BP to some extent. A composite BTME can be slightly better to serve the cooling needs of the BP compared to the hybrid BTMS. The approach to integrate multiple cooling methods and select/develop new cooling media for further comprehensive improvement of the BTMS should be considered in future research.

**Acknowledgments:** This work was supported by the J. J. Lohr College of Engineering and the Department of Mechanical Engineering at South Dakota State University, which is gratefully acknowledged.

## References

1. Friedlingstein, P., O'Sullivan, M., Jones, M. W., Andrew, R. M., Bakker, D. C. E., Hauck, J., Landschützer, P., Le Quéré, C., Luijkx, I. T., Peters, G. P., Peters, W., Pongratz, J., Schwingshackl, C., Sitch, S., Canadell, J. G., Ciais, P., Jackson, R. B., Alin, S. R., Anthoni, P., Barbero, L., Bates, N. R., Becker, M., Bellouin, N., Decharme, B., Bopp, L., Brasika, I. B. M., Cadule, P., Chamberlain, M. A., Chandra, N., Chau, T.-T.-T., Chevallier, F., Chini, L. P., Cronin, M., Dou, X., Enyo, K., Evans, W., Falk, S., Feely, R. A., Feng, L., Ford, D. J., Gasser, T., Ghattas, J., Gkritzalis, T., Grassi, G., Gregor, L., Gruber, N., Gürses, Ö., Harris, I., Hefner, M., Heinke, J., Houghton, R. A., Hurtt, G. C., Iida, Y., Ilyina, T., Jacobson, A. R., Jain, A., Jarníková, T., Jersild, A., Jiang, F., Jin, Z., Joos, F., Kato, E., Keeling, R. F., Kennedy, D., Klein Goldewijk, K., Knauer, J., Korsbakken, J. I., Körtzinger, A., Lan, X., Lefèvre, N., Li, H., Liu, J., Liu, Z., Ma, L., Marland, G., Mayot, N., McGuire, P. C., McKinley, G. A., Meyer, G., Morgan, E. J., Munro, D. R., Nakaoka, S.-I., Niwa, Y., O'Brien, K. M., Olsen, A., Omar, A. M., Ono, T., Paulsen, M., Pierrot, D., Pocock, K., Poulter, B., Powis, C. M., Rehder, G., Resplandy, L., Robertson, E., Rödenbeck, C., Rosan, T. M., Schwinger, J., Séférian, R., Smallman, T. L., Smith, S. M., Sospedra-Alfonso, R., Sun, Q., Sutton, A. J., Sweeney, C., Takao, S., Tans, P. P., Tian, H., Tilbrook, B., Tsujino, H., Tubiello, F., van der Werf, G. R., van Ooijen, E., Wanninkhof, R., Watanabe, M., Wimart-Rousseau, C., Yang, D., Yang, X., Yuan, W., Yue, X., Zaehle, S., Zeng, J., and Zheng, B.: Global carbon budget 2023, *Earth System Science Data* **2023**, 15(12), 5301–5369.
2. Mehmood, K. A., ul Hassan, J., Hassan, A., Arshad, M. W., Batool, S. Consumer's automobile purchase: a concept. *Qlantic Journal of Social Sciences and Humanities* **2024**, 5(1), 203-207.
3. International Energy Agency. Global EV Outlook 2023 – Catching up with climate ambitions. 2023. Source: IEA. International Energy Agency Website: www.iea.org.
4. Xia, G., Cao, L., Bi, G. A review on battery thermal management in electric vehicle application. *Journal of Power Sources* **2017**, *367*, 90–105.
5. Waldmann, T., Wilka, M., Kasper, M., Fleischhammer, M., Wohlfahrt-Mehrens, M. Temperature dependent ageing mechanisms in Lithium-ion batteries – a post-mortem study. *Journal of power sources* **2014**, 262, 129-135.
6. Song, L., Zheng, Y., Xiao, Z., Wang, C., Long, T. Review on thermal runaway of lithium-ion batteries for electric vehicles. *Journal of Electronic Materials* **2022**, 51(1), 30-46.
7. Shim, J., Kostecki, R., Richardson, T., Song, X., Striebel, K. Electrochemical analysis for cycle performance and capacity fading of a lithium-ion battery cycled at elevated temperature. *Journal of Power Sources* **2022**, 112(1), 222–230.
8. Lv, S., Wang, X., Lu, W., Zhang, J., Ni, H. The influence of temperature on the capacity of lithium ion batteries with different anodes. *Energies* **2022**, 15(1), 60.
9. Al-Zareer, M., Dincer, I., Rosen, M. A. A novel approach for performance improvement of liquid to vapor based battery cooling systems. *Energy Conversion and Management* **2019**, 187, 191-204.
10. Song, W., Chen, M., Bai, F., Lin, S., Chen, Y., Feng, Z. Non-uniform effect on the thermal/aging performance of Lithium-ion pouch battery. *Applied Thermal Engineering* **2018**, 128, 1165-1174.
11. Klein, M., Tong, S., Park, J. W. In-plane nonuniform temperature effects on the performance of a large-format lithium-ion pouch cell. *Applied Energy* **2016**, 165, 639-647.
12. Thawkar, V., Dhoble, A. S. A review of thermal management methods for electric vehicle batteries based on heat pipes and PCM. *Journal of the Brazilian Society of Mechanical Sciences and Engineering* **2023**, 45(2), 90.
13. Ma, S., Jiang, M., Tao, P., Song, C., Wu, J., Wang, J., Deng, T., Shang, W. Temperature effect and thermal impact in lithium-ion batteries: a review. *Progress in Natural Science: Materials International* **2018**, 28(6), 653-666.
14. Wu, W., Wang, S., Wu, W., Chen, K., Hong, S., Lai, Y. A critical review of battery thermal performance and liquid based battery thermal management. *Energy Conversion Management* **2019**, 182, 262–281.

15. Li, K, Yan, J, Chen, H, Wang, Q. Water cooling based strategy for lithium-ion battery pack dynamic cycling for thermal management system. *Applied Thermal Engineering* **2018**, 132, 575–85.
16. Waldmann, T., Wilka, M., Kasper, M., Fleischhammer, M., Wohlfahrt-Mehrens, M. Temperature dependent ageing mechanisms in lithium-ion batteries—a post-mortem study. *J Power Sources* **2014**, 262, 129-135.
17. Kabir, M. M., Demirocak, D. E. Degradation mechanisms in Li-ion batteries: a state-of-the-art review. *International Journal of Energy Research* **2017**, 41(14), 1963-1986.
18. Arora, S. Selection of thermal management system for modular battery packs of electric vehicles: a review of existing and emerging technologies. *Journal of Power Sources* **2018**, 400, 621–640.
19. Andwari, A. M., Pesiridis, A, Rajoo, S, Martinez-Botas, R, Esfahanian, V. A review of Battery Electric Vehicle technology and readiness levels. *Renewable and Sustainable Energy Reviews* **2017**, 78, 414–430.
20. Kim, J., Oh, J., Lee, H. Review on battery thermal management system for electric vehicles. *Applied Thermal Engineering* **2018**, 149, 192–212.
21. Khan, M. R., Swierczynski, M. J., Kær, S. K. Towards an ultimate battery thermal management system: a review. Batteries 2017, 3(1), 9.
22. Garud, K. S., Tai, L. D., Hwang, S.-G., Nguyen, N.-H., Lee, M.-Y. A review of advanced cooling strategies for battery thermal management systems in electric vehicles. *Symmetry* **2023**, 15, 1322.
23. Hwang, F. S., Confrey, T., Reidy, C., Picovici, D., Callaghan, D., Culliton, D., Nolan, C. Review of battery thermal management systems in electric vehicles. *Renewable and Sustainable Energy Reviews* **2024**, 192, 114171.
24. Dhage, A. Types of battery thermal management systems. Battery Design – from Chemistry to pack February 18, 2024. Accessed online at Types of Battery thermal management Systems - Battery Design on April 6, 2024.
25. Zhao, C., Zhang, B., Zheng, Y., Huang, S., Yan, T., Liu, X. Hybrid battery thermal management system in electric vehicles: a review. *Energies* **2020**, 13(23), 6257.
26. Jomde, A., Patane, P., Nadgire, A., Patil, C., Kolas, K., Bhojwani, V. Battery Thermal Management System for EVs: A Review. In: Mathew, V.K., Hotta, T.K., Ali, H.M., Sundaram, S. (eds) Energy Storage Systems. Engineering Optimization: Methods and Applications. 2023, Springer, Singapore.
27. Lin, Y., Chen, Y.-W., Yang, J.-T. Optimized thermal management of a battery energy-storage system (BESS) inspired by air-cooling inefficiency factor of data centers. *International Journal of Heat and Mass Transfer* **2023**, 200, 123388.
28. Al-Zareer, M., Dincer, I., Rosen, M. A. Electrochemical modeling, and performance evaluation of a new ammonia-based battery thermal management system for electric and hybrid electric vehicles. *Electrochimica Acta* **2017**, 247, 171–182.
29. Zhang, S., Zhao, R., Liu, J., Gu, J. Investigation on a hydrogel based passive thermal management system for lithium-ion batteries. *Energies* **2014**, 68, 854–861.
30. Wang, J., Gan, Y., Liang, J., Tan, M., Li, Y. Sensitivity analysis of factors influencing a heat pipe-based thermal management system for a battery module with cylindrical cells. *Applied Thermal Engineering* **2019**, 151, 475-85.
31. Wu, W., Liu, J., Liu, M., Rao, Z., Deng, H., Wang, Q., Qi, X., Wang, S. An innovative battery thermal management with thermally induced flexible phase change material. *Energy Conversion and Management* **2020**, 221, 113145.
32. Yue, Q., He, C., Jiang, H., Wu, M., Zhao, T. A hybrid battery thermal management system for electric vehicles under dynamic working conditions. *International Journal of Heat and Mass Transfer* **2021**, 164, 120528.
33. Ma, K., Liu, J. Liquid metal cooling in thermal management of computer chips. *Frontiers of Energy and Power Engineering in China* **2007**, 1, 384–402.
34. Ma, K.-Q., Liu, J. Heat-driven liquid metal cooling device for the thermal management of a computer chip. *Journal of Physics D: Applied Physics* **2007**, 40, 4722–4729.
35. Huo, Y., Rao, Z. The numerical investigation of nanofluid based cylinder battery thermal management using lattice Boltzmann method. *International Journal of Heat and Mass Transfer* **2015**, 91, 374–384.
36. Wang, T., Tseng, K. J., Zhao, J., Wei, Z. Thermal investigation of lithium-ion battery module with different cell arrangement structures and forced air-cooling strategies. *Applied Energy* **2014**, 134, 229-238.

37. Tang, Y., Jia, M., Li, J., Lai, Y., Cheng, Y., Liu, Y. (2014). Numerical Analysis of Distribution and Evolution of Reaction Current Density in Discharge Process of Lithium-Ion Power Battery. *Journal of the Electrochemical Society* **2014**, *161*(8), E3021–E3027.
38. Chacón, X. C. A., Laureti, S., Ricci, M., Cappuccino, G. A review of non-destructive techniques for lithium-ion battery performance analysis. *World Electric Vehicle Journal* **2023**, 14(11), 305.
39. Ping, P., Wang, Q., Huang, P., Sun, J., Chen, C. Thermal behaviour analysis of lithium-ion battery at elevated temperature using deconvolution method, *Applied Energy* **2014**, 129, 261-273.
40. Feng, X., Sun, J., Ouyang, M., He, X., Lu, L., Han, X., Fang, M., Peng, H. Characterization of large format lithium ion battery exposed to extremely high temperature. *Journal of Power Sources* **2014**, 272, 457-467.
41. Aruna, P., Vasan Prabhu, V., Krishnakumar, V., Velmurugan, P. Review on Lithium-Ion Battery Modeling Techniques for Electric Vehicle Applications. In: Dhar, S., Do, D.-T., Sur, S. N., Liu, C.-M. (eds) Advances in Communication, Devices and Networking. ICCDN 2022. Lecture Notes in Electrical Engineering, 2023, vol. 1037, 551-565, Springer, Singapore. https://doi.org/10.1007/978-981-99-1983-3_49.
42. Olsen, N. R. B. CFD algorithms for hydraulic engineering. Department of Hydraulic and Environmental Engineering, The Norwegian University of Science and Technology, 80 pages, 2000.
43. Versteeg, H. K., Malalasekera, W. An introduction to computational fluid dynamics, 1st edn. 1995, Longman Science & Technical, Harlow.
44. Shih, T.-H., Liou, W. W., Shabir, A., Yang, A., Zhu, J. A new k-ε Eddy-viscosity model for high Reynolds number turbulent flows-model development and validation, *Computers & Fluids* **1995**, 24(3), 227-238.
45. Bulat, M. P., Bulat, P. V. Comparison of turbulence models in the calculation of supersonic separated flows. *World Applied Sciences Journal* **2013**, 27(10), 1263–1266.
46. ANSYS, Inc. Ansys Fluent Theory Guide 2022/R1, 2022, Ansys, Inc., Canonsburg, PA, USA.
47. Sun, J., Dan, D., Wei, M., Cai, S., Zhao, Y., Wright, E. Pack-level modeling and thermal analysis of a battery thermal management system with phase change materials and liquid cooling. Energies 2023, 16(15), 5815.
48. Ye, J., Aldaher, A. Y. M., Tan, G. Thermal performance analysis of 18,650 battery thermal management system integrated with liquid-cooling and air-cooling. *Journal of Energy Storage* **2023**, 72, 108766.
49. Xia, B., Liu, Y., Huang, R., Yang, Y., Lai, Y., Zheng, W., Wang, H., Wang, W., Wang, M. Thermal analysis and improvements of the power battery pack with liquid cooling for electric vehicles. *Energies* **2019**, 12(16), 3045.
50. EVE, LF50F, access the website on April 19, 2024, at LF50F (evemall.com).
51. Bernardi, D., Pawlikowski, E., Newman, J. A general energy balance for battery systems. *Journal of The Electrochemical Society* **1985**, 132(1), 5-12.
52. Sagar, P., Teotia, P., Sahlot, A. D., Thakur, H. C. Heat transfer analysis and optimization of engine fins of varying surface roughness. *Materials Today: Proceedings* **2017**, *4*(8), 8565-8570.
53. Yu, M., Modesti, D., Pirozzoli, S. Direct numerical simulation of flow in open rectangular ducts. *Journal of Fluid Mechanics* **2023**, *977*, A32.
54. Wang, X., Liang, X., Hao, Z., Chen, R. Comparison of electrical and mechanical water pump performance in internal combustion engine. International Journal of Vehicle Systems Modeling and Testing **2015**, 10(3), 205-223.
55. Zhang, L., Li, J., Feng, Z., Peng, S., Zhao, S. Research on multi-objective optimization of automotive electronic water pump motor considering the factor of gap viscous loss. Structural and Multidisciplinary Optimization **2022**, 65(9), 243.
56. Bhagavathy, S. M., Budnitz, H., Schwanen, T., McCulloch, M. Impact of charging rates on electric vehicle battery life. *Findings* **2021**, March, 5 pages. DOI:10.32866/001c.21459.